



Lattice Boltzmann modelling and study of droplet equatorial streaming in an electric field

Geng Wang¹, Timan Lei¹, Junyu Yang¹, Linlin Fei², Jin Chen¹ and Kai H. Luo^{1,†}

¹Department of Mechanical Engineering, University College London, Torrington Place, London WC1E 7JE, UK

²Chair of Building Physics, Department of Mechanical and Process Engineering, ETH Zürich (Swiss Federal Institute of Technology in Zürich), Zürich 8092, Switzerland

(Received 16 December 2023; revised 25 March 2024; accepted 29 April 2024)

In 2017, Brosseau & Vlahovska (*Phys. Rev. Lett.*, vol. 119, no. 3, 2017, p. 034501) found that, in a strong electric field, a weakly conductive, low-viscosity droplet immersed in a highly conductive, high-viscosity medium formed a lens shape, and liquid rings continuously detached from its equatorial plane and subsequently broke up into satellite droplets. This fascinating multiphase electrohydrodynamic (EHD) phenomenon is known as droplet equatorial streaming. In this paper, based on the unified lattice Boltzmann method framework proposed by Luo *et al.* (*Phil. Trans. R. Soc. A Math. Phys. Engng Sci.*, vol. 379, no. 2208, 2021, p. 20200397), a novel lattice Boltzmann (LB) model is constructed for multiphase EHD by coupling the Allen–Cahn type of multiphase LB model and two new LB equations to solve the Poisson equation of the electric field and the conservation equation of the surface charge. Using the proposed LB model, we successfully reproduced, for the first time, the complete process of droplet equatorial streaming, including the continuous ejection and breakup of liquid rings on the equatorial plane. In addition, it is found that, under conditions of high electric field strength or significant electrical conductivity contrast, droplets exhibit fingering equatorial streaming that was unknown before. A power-law relationship is discovered for droplet total charge evolution and a theoretical model is then proposed to describe the droplet radius and height over time. The breakup of liquid rings is found to be dominated by capillary instability, while the breakup of liquid fingers is governed by the end-pinching mechanism. Finally, a phase diagram is constructed for fingering equatorial streaming and ring equatorial streaming, and a criterion equation is established for the phase boundary.

Key words: electrohydrodynamic effects, breakup/coalescence

† Email address for correspondence: k.luo@ucl.ac.uk

1. Introduction

The foundational studies on multiphase electrohydrodynamics (EHD) can be traced back to the work of Rayleigh (1882), who discovered that a charged drop exhibits instability and the ejection of satellite droplets from the cone of the droplet, a phenomenon known as Coulomb fission (Stuart 1985; Duft *et al.* 2003; Fernández de la Mora 2007). Subsequently, Taylor (1964) discovered that, under a strong external electric field, a liquid cone would be stretched parallel to the field, generating jet streaming from the conical tip. The seminal review by Melcher & Taylor (1969) has generated considerable research interest in the field. In particular, Allan *et al.* (1962) found that a weakly conductive dielectric droplet subjected to an electric field not only deforms parallel to the field (prolate) but also deforms perpendicular to the field direction (oblate). Over the subsequent decades, continuous experimental (Ha & Yang 2000; Reznik *et al.* 2004; Achtzehn *et al.* 2005) and theoretical research (Stuart 1985; Reznik *et al.* 2004; Betelú *et al.* 2006) has provided new physical insights, establishing the foundation for wide application of multiphase EHD (Zhang *et al.* 2023). One of the most representative applications of multiphase EHD is electrospray mass spectrometry (Fenn *et al.* 1989, 1990), which contributed to Finn winning the Nobel Prize in Chemistry in 2002. In contrast to the theoretical and experimental advancements, numerical simulation research on multiphase EHD has progressed relatively slowly (Vlahovska 2019; Wagoner *et al.* 2021). While Taylor, McEwan & de Jong (1966) first proposed the leaky dielectric model (LDM) in their paper over 50 years ago, simulations specifically addressing Coulomb fission did not appear until 2008 (Collins *et al.* 2008).

Extensive research has been conducted on the prolate breakup of the droplets (Vlahovska 2019), especially for Coulomb fission (Fernández de la Mora 2007). Rayleigh (1882) predicted that instability occurs when the droplet carries a charge greater than $q_c = 8\pi\sqrt{\gamma\varepsilon R_0^3}$ (R_0 is the initial radius of the droplet, ε is dielectric permittivity, γ is surface tension). Subsequent experiments (Bentley & Leal 1986; Karyappa, Deshmukh & Thaokar 2014) revealed that, besides the jetting from the tips, prolate deformation of droplets can result in various breakup outcomes, such as lobes breaking and open jets. Additionally, some experimental studies researched Coulomb fission for non-Newtonian droplets (Ha & Yang 2000; Mandal & Chakraborty 2017) and droplets containing surfactants (Eggleton, Tsai & Stebe 2001; Luo *et al.* 2017). Another interesting topic in Coulomb fission is the charge and mass loss of the droplet (Fernández de la Mora 2007). Duft *et al.* (2003) first provided high-resolution experimental images for charged droplet Coulomb fission, indicating that the droplet's charge loss is approximately 33 % of the total charge, with a mass loss less than 1 %. A subsequent numerical study by Gawande, Mayya & Thaokar (2017) has confirmed this experimental discovery. Interest in Coulomb fission has sparked numerous numerical studies (Giglio *et al.* 2008; Burton & Taborek 2011; Mandal & Chakraborty 2017; Sengupta, Walker & Khair 2017; Li *et al.* 2023) aiming to simulate the droplet prolate breakup in an electric field. Collins *et al.* (2008, 2013) first proposed a scaling law for the radius of ejected droplets and the charge quantity in EHD tip streaming. Subsequently, Gawande, Mayya & Thaokar (2019, 2022) investigated the effect of electrical conductivity on the breakup mechanisms for prolate deformation of droplets. Sengupta *et al.* (2017) explored the impact of charge convection on the breakup mechanism of charged droplets, suggesting that the tip-streaming phenomenon occurs only with finite electric conductivity.

Unlike the prolate fission of droplets in an electric field, the oblate fission of droplets has only gained widespread attention in recent years (Vlahovska 2019; Marin 2020). Brosseau & Vlahovska (2017) in their groundbreaking experiment discovered that, in a strong electric field, a droplet placed in a medium with higher electric conductivity and

permittivity, and lower viscosity, experiences central collapse, leading to an uncontrolled fragmentation. Conversely, when the droplet's viscosity is orders of magnitude smaller than the external medium, it forms a lens-like shape and produces continuously detached liquid rings at the equator. As the liquid rings break, over a hundred satellite droplets are generated in the equatorial plane of the mother droplet, a phenomenon now known as equatorial streaming (Vlahovska 2019; Marin 2020). In fact, Mohamed *et al.* (2016) have found similar phenomena before, where they observed a fragmented liquid ring to form around the droplet perpendicular to the imposed field. This fascinating phenomenon quickly attracted a great deal of interest from researchers due to its ability to produce a large number of size-controllable satellite droplets. Wagoner *et al.* (2020) solved the steady-state solutions of the LDM equations and obtained the steady shapes of collapsed and lens-shaped droplets, providing a theoretical explanation for the different breakup mechanisms. After that, Firouznia *et al.* (2022) used linear analysis to explore the nonlinear effects generated by the coupling of flowing interfaces and the charge dynamics. More recently, Wagoner *et al.* (2021) extended their study to transient simulations, indicating that the lens-shaped droplet becomes unstable only with charge relaxation and charge convection. However, research on droplet equatorial streaming is still in its early stage, and there is a lack of a comprehensive understanding of the underlying physics (Wagoner *et al.* 2021). It is also noted that numerical studies replicating the detachment and breakup of liquid rings in equatorial streaming have not been reported.

Currently, simulation methods for multiphase EHD problems mainly include the boundary element method (Betelú *et al.* 2006; Garzon, Gray & Sethian 2014; Gawande *et al.* 2017, 2019), the finite element method (Collins *et al.* 2008, 2013; Tian *et al.* 2022; Misra & Gamero-Castaño 2023), EHD–volume of fluid (VOF) method (López-Herrera, Popinet & Herrada 2011; López-Herrera *et al.* 2015) and the lattice Boltzmann method (LBM) (Zhang & Kwok 2005; Gong, Cheng & Quan 2010; Cui, Wang & Liu 2019; Liu, Chai & Shi 2019; Luo *et al.* 2020). Collins *et al.* (2008, 2013) successfully employed the finite element method to simulate Coulombic fission for the first time. However, simulating droplet fission in an electric field remains a highly challenging task. For example, boundary element methods often suffer from numerical instability, partly because the droplet's tip becomes singular at the critical moment of fragmentation, where the curvature and the capillary force become infinite. Therefore, existing studies (Gawande *et al.* 2017; Sengupta *et al.* 2017) typically focus on the behaviours of droplets at the critical moments of fission. The EHD–VOF model has been widely employed in simulating electrohydrodynamic atomization phenomena (López-Herrera *et al.* 2011; Herrada *et al.* 2012). Mohamed *et al.* (2016) investigated the fragmentation of suspended droplets above the critical electric field through experiments and numerical simulations, and observed the novel splashing and split-splashing phenomena. They successfully reproduced the droplet splashing using an axisymmetric EHD–VOF model. Recently, López-Herrera, Herrada & Gañán-Calvo (2023) numerically investigated the cone-jet electrosprays of a fully dissociated electrolyte, providing a detailed discussion of the ion concentration of effects.

In existing lattice Boltzmann simulations, charge relaxation and charge convection are usually ignored, with a focus on the situation of infinite electric conductivity (Cui *et al.* 2019; Liu *et al.* 2019). Also, due to the high computational cost of solving the Poisson equation for the electric field, the majority of simulations are limited to two dimensions (Zhang & Kwok 2005; Cui *et al.* 2019; Liu *et al.* 2019; Luo *et al.* 2020). There is an urgent need to develop a new numerical methodology to simulate the entire process of droplet equatorial streaming. Recently, Luo, Fei & Wang (2021) proposed a unified

lattice Boltzmann model (ULBM) that integrates commonly used collision operators into a unified framework. The ULBM allows for easy switching between different advanced collision operators while facilitating the extension of LB models for new multiphysics phenomena. Due to its generality and flexibility, the ULBM is well suited for the multiphase flow and coupled multiphysics problems (Wang, Fei & Luo 2022*b*; Wang *et al.* 2023).

This research aims to numerically investigate the droplet equatorial streaming in an electric field, filling the gap in the simulation of the entire process of this novel phenomenon. In particular, the paper attempts to answer three main questions: (i) whether different breakup mechanisms exist for droplets in a wider range of parameters than in experiments, (ii) how the radius and charge of droplets evolve during equatorial streaming and (iii) what the mechanisms are for the breakup of the liquid ring and the distribution of satellite droplets. To address these questions, a novel multiphase EHD model that considers charge relaxation and charge convection is developed based on the ULBM framework. In order to capture the dynamics of the equatorial streaming process of the entire droplet, fully three-dimensional simulations are conducted. In the following § 2, the governing equations of the problem and the proposed LBM model are introduced. Comprehensive validations and sensitivity analyses of the model are described in § 3. In § 4, we systematically investigate the equatorial flow of liquid droplets, focusing on the breakup outcomes, dynamic evolution and the generation of satellite droplets for a wider range of operation parameters. The conclusions of this study are presented in § 5.

2. Physical and numerical models

2.1. Governing equations for EHD

In this work, the governing equations involving EHD have the following assumptions. First, both the internal medium and the external medium of the droplet are immiscible and incompressible. Second, consistent with experiment (Brosseau & Vlahovska 2017), both media are treated as Newtonian fluids with constant physical properties without the influence of gravity. Thirdly, the two-phase EHD is described by the LDM, where the surface charge is treated as the volumetric charge within the interfacial diffusion layer. We assume charge accumulation at the phase interface while no charges exist in the bulk fluid. On the interface, a balance is achieved among surface charges through a competition between the ohmic conduction mechanism, the charge convection mechanism and charge diffusion. To simulate the two-phase flow, the phase-field model is employed, and an improved conservative Allen–Cahn (AC) equation, which was originally proposed in the work of Allen & Cahn (1979), is used for interface tracking (Jain 2022; Liang *et al.* 2023)

$$\frac{\partial \phi}{\partial t} + \nabla \cdot (\phi \mathbf{u}) = \nabla \cdot M_\phi \left(\nabla \phi - \frac{\mathbf{n}}{w} \left[1 - \tanh^2 \left(\frac{2T}{w} \right) \right] \right), \quad (2.1)$$

where ϕ is the phase indicator, for the heavy phase $\phi_h = 1.0$ and for the light phase $\phi_l = 0$, with $\phi_0 = (\phi_h + \phi_l)/2 = 0.5$ indicating the position of the interface. Also, \mathbf{n} is the unit vector normal to the interface, which is calculated by $\mathbf{n} = \nabla \phi / |\nabla \phi|$, M_ϕ is the mobility and w stands for the interface thickness; $\mathbf{u} = [u_x, u_y, u_z]$ is the fluid velocity. Different from the traditional AC equation, a signed-distance function T is introduced to avoid any jumps or discontinuities at the interface, where

$$T = \frac{w}{4} \ln \left(\frac{\phi}{1 - \phi} \right). \quad (2.2)$$

For the phase-field multiphase model, the conservative AC equation is coupled with incompressible Navier–Stokes (NS) equations, and the continuity and momentum equations for incompressible multiphase flows can be expressed as (Unverdi & Tryggvason 1992)

$$\left. \begin{aligned} \nabla \cdot \mathbf{u} &= 0, \\ \frac{\partial(\rho \mathbf{u})}{\partial t} + \nabla \cdot (\rho \mathbf{u} \mathbf{u}) &= -\nabla P + \nabla \cdot \left(\rho \nu (\nabla \mathbf{u} + \nabla \mathbf{u}^T) + \rho \left(\nu_b - \frac{2}{3} \nu \right) (\nabla \cdot \mathbf{u}) \mathbf{I} \right) + \mathbf{F}_s + \mathbf{F}_e, \end{aligned} \right\} \quad (2.3)$$

where ρ indicates the fluid density, ν is the fluid kinematic viscosity, ν_b stands for the non-hydrodynamic bulk viscosity and P is the pressure; \mathbf{F}_s , \mathbf{F}_e are the surface tension and external electric force, respectively,

$$\mathbf{F}_s = \mu_\phi \nabla \phi, \quad (2.4a)$$

$$\mathbf{F}_e = \rho_e \mathbf{E} - \frac{1}{2} \mathbf{E}^2 \nabla \varepsilon, \quad (2.4b)$$

where $\mu_\phi = 4\beta(\phi - \phi_l)(\phi - \phi_h)(\phi - \phi_0) - k\nabla^2\phi$ is the chemical potential, and the parameters $\beta = 12\gamma/w$ and $k = 3\gamma w/2$ are related to the interface thickness w and the surface tension γ . The first term in external electric force \mathbf{F}_e stands for the Coulomb force and the second term represents the dielectric force (Melcher & Taylor 1969; Tomar *et al.* 2007).

For the electric field, the governing equation of the field strength follows Gauss’s law

$$\nabla \cdot (\varepsilon \nabla \psi) = -\rho_e, \quad (2.5)$$

where ψ is the electric potential, and ρ_e is the charge density. The electric field strength is given as

$$\mathbf{E} = -\nabla \psi. \quad (2.6)$$

In this work, we consider a non-zero bulk charge model. The charge is represented by charge density ρ_e , which indicates the concentration of all existing ions (Gañán-Calvo *et al.* 2018). The evolution of charge density is resolved on the phase diffusion interface. Similar charge density assumptions have been successfully applied in modelling using the EHD–VOF method (López-Herrera *et al.* 2011). The governing equation for the charge density evolution can be described as the following charge conservation equation (Melcher & Taylor 1969; Vlahovska 2019):

$$\frac{\partial \rho_e}{\partial t} + \nabla \cdot (\rho_e \mathbf{u}) - \nabla \cdot (\sigma \nabla \psi) - \alpha \nabla^2 \rho_e = 0, \quad (2.7)$$

where α is the charge diffusion number and σ is the fluid electric conductivity. From the left to the right of the above equation, the first term stands for the charge relaxation, the second term accounts for charge convection, the third term stands for the ohmic conduction and the last term represents the charge diffusion. By introducing characteristic variables $l_{ch} = R_0$, $u_{ch} = \varepsilon_{ex} R_0 E_0^2 / \mu_{ex}$, $t_{ch} = t_{diff} = \mu_{ex} R_0 / \gamma$, $\rho_{ech} = \varepsilon_{ex} E_0$, $\sigma_{ch} = \sigma_{ex}$ and $\alpha_{ch} = \varepsilon_{ex} R_0^2 E_0^2 / \mu_{ex}$, where the subscript *ex* refers to the external phase of the droplet, and E_0 is the electric field strength, the above charge conservation equation can be normalized as

$$\frac{t_e}{t_{diff}} \frac{\partial \rho_e^*}{\partial t^*} + \frac{t_e}{t_{conv}} \nabla \cdot (\rho_e^* \mathbf{u}^*) - \nabla \cdot (\sigma^* \nabla \psi^*) - \alpha^* \nabla^2 \rho_e^* = 0, \quad (2.8)$$

where $t_e = \varepsilon_0 / \sigma_0$ stands for the time scale of charge relaxation, $t_{conv} = R_0 / u_{ch}$ stands for the time scale of charge convection and $\alpha^* = \alpha \mu_0 / (\varepsilon_0 R_0^2 E_0^2)$ is the dimensionless charge

diffusion number. Previous studies (Collins *et al.* 2008, 2013) indicated that, when α^* is less than 10^{-3} , charge diffusion has no significant impact on the results; in the following simulations α^* is set as 10^{-4} .

In most previous simulations of two-phase EHD, the charge density is assumed to be relaxed immediately as the electric field changes, i.e. $t_e \rightarrow 0$ (Luo *et al.* 2020). Subsequently, the charge relaxation and the charge convection are ignored. Considering that the charge diffusion is usually negligible compared with the ohmic conduction, the above charge conservation equation can be simplified as $\nabla \cdot (\sigma \nabla \psi) = 0$. However, Wagoner *et al.* (2021) theoretically proved that the instability at the equator is only triggered when considering the convection and relaxation of surface charge. Additionally, both Sengupta *et al.* (2017) and Wagoner *et al.* (2020) reported that the jetting of sub-droplets only occurs under finite electric Reynolds numbers ($Re_e = t_e/t_{conv}$). When Re_e approaches 0, the droplet exhibits an end-pinching state with conical ends. In this study, we focus on the cone jetting at the equator, which is a problem with Re_e in the range of $10 \sim 10^5$, $t_{diff} \sim 10^{-3}$ s and $t_{conv} \sim 10^{-4}$ s are of similar magnitude. Therefore, the charge relaxation and charge convection dominate over charge diffusion, and the complete charge conservation equation (2.7) will be solved.

2.2. The ULBM algorithm for the governing equations

In this work, the ULBM framework proposed by Luo *et al.* (2021) is employed to solve the above governing equations. Since the introduction of the ULBM framework, it has been widely applied in simulating various multiphase flows (Yang *et al.* 2021; Wang *et al.* 2022b, 2023), and phase-change problems (Wang *et al.* 2022a; Fei *et al.* 2023). As a general framework covering different collision models, multiphase flow models and force schemes, it has inherent advantages in simulating multiphase flows coupled with multiple physical fields. The general collision equation for the ULBM model can be expressed as (Luo *et al.* 2021; Wang *et al.* 2022b)

$$f_i(\mathbf{x} + \mathbf{e}_i \Delta t, t + \Delta t) = f_i^*(\mathbf{x}, t) = \mathbf{M}^{-1} \mathbf{N}^{-1} (\mathbf{I} - \mathbf{S}) \mathbf{N} \mathbf{M} f_i(\mathbf{x}, t) + \mathbf{M}^{-1} \mathbf{N}^{-1} \mathbf{S} \mathbf{N} f_i^{eq}(\mathbf{x}, t) + \Delta t \mathbf{M}^{-1} \mathbf{N}^{-1} (\mathbf{I} - \mathbf{S}/2) \mathbf{N} \mathbf{M} C_i, \quad (2.9)$$

where f_i and f_i^* are the pre-collision and post-collision distribution functions, respectively, f_i^{eq} is the equilibrium distribution function and C_i is the external forcing term; \mathbf{e}_i and $\Delta t = 1$ are the discrete velocities and the time step, respectively, and \mathbf{I} stands for the unit matrix.

The generality and universality of the ULBM model are achieved through the implementation of three different matrices: the transformation matrix \mathbf{M} is used to transform the distribution functions (f_i) to their raw moments (\mathbf{m}), and the shift matrix \mathbf{N} is used to convert the raw moment collision into the central moment space ($\tilde{\mathbf{m}}$), the transformation/shift can be expressed as (Fei & Luo 2017; Fei, Luo & Li 2018)

$$\tilde{\mathbf{m}} = \mathbf{N} \mathbf{m} = \mathbf{N} \mathbf{M} f_i. \quad (2.10)$$

Finally, the relaxation matrix \mathbf{S} contains the relaxation parameters which correspond to various models. Through these three matrices, the ULBM model can facilitate the switch between single-relaxation-time collision models (SRT), multiple-relaxation-time collision models (MRT) (Fei *et al.* 2019), cascaded lattice Boltzmann models (Fei *et al.* 2018) and entropy lattice Boltzmann models (Karlin, Bösch & Chikatamarla 2014; Bösch, Chikatamarla & Karlin 2015).

In this work, the recently proposed non-orthogonal MRT phase-field ULBM model (ULBM (NMRT) PF) by Wang *et al.* (2023) is adopted to address the aforementioned phase field multiphase model. To capture the realistic dynamic behaviours of droplets in three dimensions, the three-dimensional nineteen-velocity (D3Q19) discrete velocity model is adopted. Two different distribution functions under the raw moment space are introduced to solve the conservation AC equation and the incompressible NS equations

$$\mathbf{m}_\phi^* = \mathbf{M}f_{\phi,i} = (\mathbf{I} - \mathbf{S}_\phi)\mathbf{m}_\phi + \mathbf{S}_\phi\mathbf{m}_\phi^{eq} + \Delta t \left(\mathbf{I} - \frac{\mathbf{S}_\phi}{2} \right) \mathbf{R}_\phi, \quad (2.11a)$$

$$\mathbf{m}_g^* = \mathbf{M}g_i = (\mathbf{I} - \mathbf{S}_g)\mathbf{m}_g + \mathbf{S}_g\mathbf{m}_g^{eq} + \Delta t \left(\mathbf{I} - \frac{\mathbf{S}_g}{2} \right) \mathbf{R}_g, \quad (2.11b)$$

where $\mathbf{m}_\phi^* = \mathbf{M}f_{\phi,i}$ is for conservation AC equation and $\mathbf{m}_g^* = \mathbf{M}g_i$ is for incompressible NS equations. For the non-orthogonal MRT collision operator, the shift matrix $\mathbf{N} = \mathbf{I}$ and the transformation matrix \mathbf{M} is chosen as the simplified non-orthogonal moment set which was originally proposed by Fei *et al.* (2018, 2019). In the above equation, \mathbf{m}^{eq} and \mathbf{R} are the discrete equilibrium moment set and discrete forcing term in the raw moment space, respectively. The details of the ULBM (NMRT) PF model can be found in the supplementary material S1, available at <https://doi.org/10.1017/jfm.2024.441>, including explicit expressions of \mathbf{m}_ϕ^{eq} , \mathbf{R}_ϕ , \mathbf{m}_g^{eq} and \mathbf{R}_g . As proven in our previous work (Wang *et al.* 2023), the above ULBM (NMRT) PF model can accurately recover the target NS equations and interface tracking equation. The ULBM (NMRT) PF has been extensively validated for various complex multiphase flow phenomena such as high density ratio droplet splash and jet spray, demonstrating excellent agreement with experimental results.

Next, the ULBM (NMRT) model is employed to solve the Poisson equation (2.5) for the electric field and the charge conservation equation (2.7) for surface charge. For the charge conservation equation, similar to the AC equation, the D3Q19 non-orthogonal model is utilized. Regarding its collision in the raw moment space, it has

$$\begin{aligned} \mathbf{m}_{\rho_e}^* = \mathbf{M}f_{\rho_e,i}^* &= (\mathbf{I} - \mathbf{S}_{\rho_e})\mathbf{m}_{\rho_e} + \mathbf{S}_{\rho_e}\mathbf{m}_{\rho_e}^{eq} + \Delta t \left(\mathbf{I} - \frac{\mathbf{S}_{\rho_e}}{2} \right) \mathbf{R}_{\rho_e} \\ &+ \Delta t \mathbf{C}_{\rho_e} + 0.5\Delta t^2 \partial_t(\mathbf{C}_{\rho_e}). \end{aligned} \quad (2.12)$$

For typical convection–diffusion equations such as (2.7), the equilibrium distribution function can be written as (Li *et al.* 2016; Lei, Wang & Luo 2021)

$$f_{\rho_e,i}^{eq} = \rho_e \omega(|\mathbf{e}_i|^2) \left[1 + \frac{\mathbf{e}_i \cdot \mathbf{u}}{c_s^2} \right], \quad (2.13)$$

where $\mathbf{u} = [u_x, u_y, u_z]$ are the velocity components in the x , y and z directions, respectively. The weights are $\omega(0) = 1/3$, $\omega(1) = 1/18$ and $\omega(2) = 1/36$ for the D3Q19 model, and $C_s = 1/\sqrt{3}$ stands for the lattice sound speed. The corresponding equilibrium moment set is

$$\mathbf{m}_{\rho_e}^{eq} = \mathbf{M}f_{\rho_e,i}^{eq} = \left[\rho_e, \rho_e u_x, \rho_e u_y, \rho_e u_z, 0, 0, 0, \rho_e, 0, 0, \rho_e u_x c_s^2, \rho_e u_x c_s^2, \rho_e u_y c_s^2, \rho_e u_z c_s^2, \right]^T. \quad (2.14)$$

External force terms are introduced to balance high-order time-related error terms

$$\mathbf{R}_{\rho_e} = \left[0, \partial_t(\rho_e u_x), \partial_t(\rho_e u_y), \partial_t(\rho_e u_z), 0, 0, 0, 0, 0, 0, \partial_t(\rho_e u_x)c_s^2, \partial_t(\rho_e u_x)c_s^2, \right]^T. \quad (2.15)$$

The time derivative is calculated by the Eulerian scheme, i.e.

$$\partial_t(\phi \mathbf{u}) = \frac{\rho_e(t)\mathbf{u}(t) - \rho_e(t - \Delta t)\mathbf{u}(t - \Delta t)}{\Delta t}. \quad (2.16)$$

Here, C_{ρ_e} is the additional term for ohmic conduction, which is given as

$$C_{\rho_e} = \mathbf{M}\omega(|\mathbf{e}_i|^2)C_{\rho_e,i} = \left[\nabla \cdot (\sigma \nabla \psi), 0, 0, 0, 0, 0, 0, \nabla \cdot (\sigma \nabla \psi), 0, 0, 0, 0, \right]^T. \quad (2.17)$$

For the ohmic conduction term, it can be expanded as $\nabla \cdot (\sigma \nabla \psi) = \nabla \sigma \nabla \psi + \sigma \nabla^2 \psi$. In this paper, for the differential terms associated with solving the electric field, a second-order lattice-based finite difference (FD) scheme is utilized for the solution, where

$$\nabla \mathbf{I} = \sum_i \frac{\omega(|\mathbf{e}_i|^2)\mathbf{I}(\mathbf{x} + \mathbf{e}_i)\mathbf{e}_i}{c_s^2}. \quad (2.18)$$

Here, \mathbf{I} represents the required differential terms (e.g. ψ, σ). For the Laplacian term of the electric potential $\nabla^2 \psi$, through Gauss’s law, it is replaced as $\nabla^2 \psi = -(\rho_e + \nabla \varepsilon \nabla \psi)/\varepsilon$. This transformation is to ensure a coupling between the Poisson equation and the charge conservation equation. Simultaneously, it guarantees the suppression of charge convection only at the phase interface, which can be a great challenge for the LB method since the interface width is typically only 4 to 5 grid points.

Consistent with previous studies (Zhang & Kwok 2005; Liu *et al.* 2019; Luo *et al.* 2020), a linear interpolation is employed for the dielectric permittivity at the interface, i.e.

$$\varepsilon = \varepsilon_l + \frac{\phi - \phi_l}{\phi_h - \phi_l}(\varepsilon_h - \varepsilon_l), \quad (2.19)$$

where ε_h and ε_l stand for the dielectric permittivity for the heavy phase and light phase, respectively. Due to the linear relationship between ε and ϕ , the deviation of ε can be directly achieved as $\nabla \varepsilon = \nabla \phi (\varepsilon_h - \varepsilon_l) / (\phi_h - \phi_l)$ for solving the Poisson equation and the charge conservation equation. On the other hand, the subsequent simulations in this paper will involve very large differences in electric conductivity. Therefore, in order to avoid charge leakage, we innovatively use exponential interpolation to calculate the electric conductivity at the interface, where

$$\ln(\sigma) = \ln(\sigma_l) + \frac{\phi - \phi_l}{\phi_h - \phi_l}(\ln(\sigma_h) - \ln(\sigma_l)). \quad (2.20)$$

Compared with the reciprocal interpolation (see, for example, Tomar *et al.* 2007; Misra & Gamero-Castaño 2023), this exponential interpolation leads to a smoother transition of the dielectric coefficient at the phase interface. Simultaneously, in the following simulations, the viscosity difference between the inner and outer phases can reach magnitudes of 10^2 , with the maximum electric Reynolds number Re_e being approximately 10^4 . At such a high electric Reynolds number, charge leakage is prone to occur in

the lower-viscosity phase. Considering that charge convection only occurs at the phase interface, a smooth limiting function $\mathbf{u}' = [1 - \tanh(2w(\phi - \phi_0))]\mathbf{u}$ is introduced for the velocity terms in (2.13) and (2.14) to eliminate charge convection in the bulk phase. In the supplementary material S3, we compared the improvement in charge leakage achieved by the above interfacial scheme with the linear interpolation approach.

The relaxation parameters are determined as $s_{\rho_e,1} = s_{\rho_e,2} = s_{\rho_e,3} = 1/(\alpha/c_s^2 + 0.5)$. Applying the Chapman–Enskog (CE) analysis in the supplementary material S2, the above ULBM (NMRT) model can recover the target charge conservation equation (2.7) without high-order error terms. Additionally, the remaining relaxation parameters within the relaxation matrix \mathcal{S}_{ρ_e} can be chosen freely, e.g. 1 in our simulations. After the collision in the raw moment space, the distribution function $f_{\rho_e,i}^*$ is reconstructed by $f_{\rho_e,i}^* = \mathbf{M}^{-1}\mathbf{m}_{\rho_e}^*$, the charge density can be calculated by

$$\rho_e = \sum_i f_{\rho_e,i}. \tag{2.21}$$

For the Poisson equation of the electric field, the three-dimensional seven-velocity (D3Q7) SRT collision operator is employed for its computation. Due to the necessity of internal iterations at each time step in solving the Poisson equation, the D3Q7 model is sufficient to meet the accuracy requirement. The collision step can be expressed as

$$f_{\psi,i}^* = f_{\psi,i} - \frac{1}{\tau_\psi}(f_{\psi,i} - f_{\psi,i}^{eq}) + \Delta t' C_{\psi,i} + 0.5\Delta t'^2 \partial_t(C_{\psi,i}), \tag{2.22}$$

where $\Delta t' = 1$ is the inner iteration time step, and the equilibrium distribution function is (Chai & Shi 2008)

$$\left. \begin{aligned} f_{\psi,0}^{eq} &= (\tilde{\omega}(|\mathbf{e}_0|^2) - 1)\psi, i = 0; \\ f_{\psi,i}^{eq} &= \tilde{\omega}(|\mathbf{e}_i|^2)\psi, \quad i = 1 \sim 6, \end{aligned} \right\} \tag{2.23}$$

for the D3Q7 model, $\tilde{\omega}(0) = 1/4$ and $\tilde{\omega}(1) = 1/8$. Thanks to the generality of the ULBM, the discrete velocities of the D3Q7 model can be obtained directly from the discrete velocity elements of the D3Q19 model ($i = 0 \sim 6$). For the additional term $C_{\psi,i}$ in (2.22), it is given by

$$C_{\psi,i} = \Lambda \frac{\tilde{\omega}(|\mathbf{e}_i|^2)(\rho_e + \nabla \varepsilon \nabla \psi)}{\varepsilon}, \tag{2.24}$$

where Λ is a free relaxation parameter and is set as 0.5 in this work. According to CE analysis, the relaxation time is calculated as $\tau_\psi = 1/(\Lambda c_s^2 + 0.5)$, and the electric potential is

$$\psi = \frac{\sum_{i=1}^6 f_{\psi,i}}{1 - \tilde{\omega}(|\mathbf{e}_0|^2)}. \tag{2.25}$$

In this paper, the residual of the electric potential across the whole simulation domain (i.e. $\epsilon = \sum |\psi(t') - \psi(t' - 1)| / \sum |\psi(t')|$) is used to determine the convergence of internal iterations at each time step. Specifically, we consider the iterations to be converged when ϵ is less than 10^{-7} when initializing the electric field, and for each subsequent transient time step, the iteration to have converged when ϵ is less than 10^{-6} .

Figure 1 illustrates the flowchart of the computational process. It is worth noting that the internal iterations for the electric field are computationally expensive. In some previous

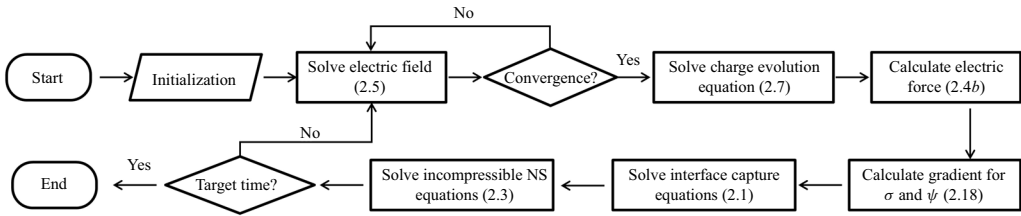


Figure 1. The flowchart of the computational procedure.

LB two-phase EHD simulations, the internal iteration step is ignored due to the small deformations of small droplets or adjustable parameters added to expedite the convergence of the Poisson equation (Luo *et al.* 2016, 2020). However, given the purpose of this study, focusing on the equatorial streaming of droplets involving significant deformation and fragmentation in an electric field, internal iterations for the electric field are retained. For a typical droplet equatorial streaming simulation, internal iterations for the electric field consume more than 50 % of the computational time.

3. Model validations

Before simulating the equatorial streaming of a droplet, we first perform validations and parameter sensitivity tests for the above models. The model is validated by four benchmarks: (i) a single-phase EHD problem; (ii) a multiphase EHD problem with a flat interface; (iii) the deformation of a droplet in an electric field; and (iv) the electrospray of a liquid droplet.

3.1. Single-phase EHD problem

The ULBM model for the charge conservation equation and the Poisson equation for the electric field are first validated by comparing the analytical solution with the numerical solution for charge density relaxation. For a single-phase flow, by neglecting charge convection and charge diffusion, Gauss’s law (2.5) and charge conservation equation (2.7) can be simplified to

$$\left. \begin{aligned} \nabla^2 \psi &= -\frac{\rho_e}{\varepsilon}, \\ \frac{\partial \rho_e}{\partial t} &= \sigma \nabla^2 \psi. \end{aligned} \right\} \quad (3.1)$$

Therefore, the charge density has the analytical solution

$$\rho_e = \rho_{e,0} \exp\left(-\frac{t}{t_e}\right). \quad (3.2)$$

The charge relaxation for three different t_e is simulated and the LB simulation results are compared with the analytical solution mentioned above. The results are shown in figure 2(a); qualitatively, our LB simulation results are in perfect agreement with the analytical solution spanning several orders of magnitude of t_e . The relative errors between the LB simulation results and analytical solutions are plotted in figure 2(b), where the relative error is defined as $\vartheta_{\rho_e} = |\rho_{e,lb} - \rho_{e,analytical}| / |\rho_{e,analytical}|$. Qualitatively, the maximum relative error between LB simulation results and analytical solutions does not exceed 0.1 %. For all cases, the relative error slightly increases in the later stages, attributed

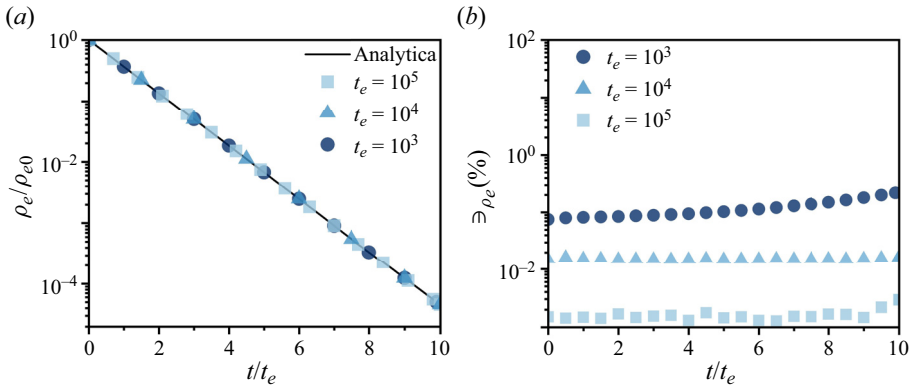


Figure 2. (a) Comparison between LB simulation results (symbols) and analytical solutions (lines) for charge density evolution in the bulk phase. (b) Time evolution of relative errors.

to the fact that the corresponding charge density has relaxed to the order of 10^{-4} of the initial charge at this stage.

3.2. Two-phase EHD problem

Next, a two-phase EHD problem with a simulation domain of size $N_x \times N_y \times N_z = 5 \times 2 \times 100$ is considered. For this case, we focus on the electric field and charge distribution in the Z direction, so it can be considered as a two-dimensional problem. Therefore, periodic boundary conditions are applied in the x and y directions, respectively, and a zero-gradient boundary condition is applied in the z direction. The lower half ($N_z < 50$) of the simulation domain represents the heavy phase, while the upper half ($N_z \geq 50$) represents the light phase, with an interface thickness of $w = 5$. On the top surface of the simulation domain, $\psi_t = 10$, and on the bottom surface, $\psi_b = 0$. For the light phase, σ_l and ε_l are kept as 0.1 and 0.001, respectively. For the heavy phase, σ_h and ε_h are changed according to the conductivity ratio $R = \sigma_h / \sigma_l$ and permittivity ratio $S = \varepsilon_h / \varepsilon_l$, respectively. Ignoring charge convection and charge diffusion, the governing equations of this two-phase EHD problem can be written as

$$\left. \begin{aligned} \nabla \cdot (\varepsilon \nabla \psi) &= -\rho_e, \\ \nabla \cdot (\sigma \nabla \psi) &= 0. \end{aligned} \right\} \quad (3.3)$$

The above equations can be solved by using a second-order FD method. In figure 3, a comparison between our LB simulation results and FD results is presented. The corresponding relative errors are recorded in table 1. Similarly to Fei *et al.* (2018), the local relative error between simulation results and FD results for the electric potential is defined as $\overline{\Xi_{\psi}} = \sum |\psi_{LB} - \psi_{FD}| / \sum |\psi_{FD}|$. As the charge density in the bulk phase is approximately 0, instead of using relative error, the total charge density difference $\Xi_{\rho_e, t} = |\sum |\rho_{e, LB}| - \sum |\rho_{e, FD}|| / \sum |\rho_{e, FD}|$ is used to quantify the error between the LB simulation results and FD results.

Figure 3(a) shows the distribution of electric potential for different values of R ranging from 0.01 to 100. It can be observed that the LB simulation results align closely with the FD solution, with differences observed only near the phase interface. Quantitatively, from table 1, it can be found that the maximum relative errors for the electric potential are less than 3% for all cases, with the relative errors being slightly increased with R . Figures 3(b) and 3(c) describe the charge density distribution at the phase interface for different R

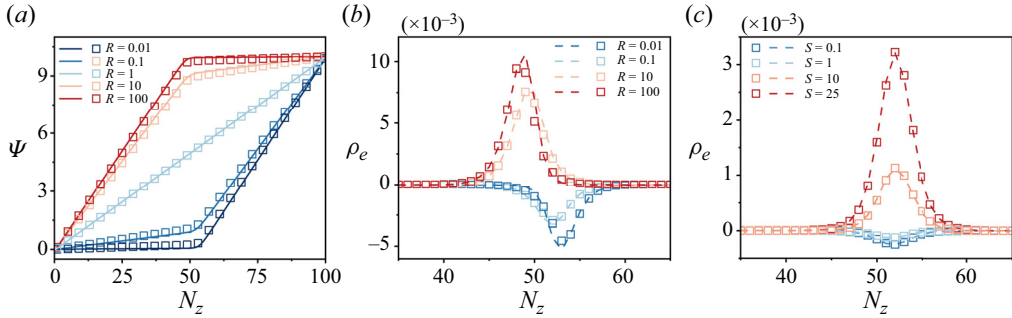


Figure 3. Comparison between LB simulation results (hollow symbols) and numerical solutions (lines) for (a) ψ for cases with different R ; (b) ρ_e at the phase interface for cases with different R ; and (c) for cases with different S .

	$S = 0.1,$ $R = 2.0$	$S = 10,$ $R = 2.0$	$S = 25,$ $R = 2.0$	$S = 2.0,$ $R = 0.01$	$S = 2.0,$ $R = 0.1$	$S = 2.0,$ $R = 100$
$\overline{\partial\psi}$	0.14 %	0.14 %	0.14 %	1.31 %	1.40 %	2.76 %
$\partial\rho_{e,t}$	0.57 %	0.20 %	0.24 %	4.23 %	4.05 %	2.72 %

Table 1. The errors between the LB simulation results and FD results for electric potential and charge density.

and S cases, respectively. For varying S , the simulation results match closely with the FD results, exhibiting a maximum relative error of 4.23 % at extreme conductivity disparities (i.e. $R = 0.01$). In the case of different S values, the LB simulation results are almost the same as the FD results, with the maximum relative errors being less than 1 %.

3.3. Deformation of a droplet in an electric field

After validating the accuracy of the electric field and the charge calculations, the simulation is extended to a two-phase EHD problem with fluid flow. Similar to previous studies (Cui *et al.* 2019; Liu *et al.* 2019; Luo *et al.* 2020), the deformation of a two-dimensional droplet in an electric field is initially simulated. The droplet's initial radius R_0 is 30, and the interface thickness $w/R_0 = 0.1$. The viscosity and density ratios between the inner and external phases are both set to 1. In this case, the permittivity ratio S is fixed at 3.5, and simulations are conducted for two different values of $R = 1.75$ and 4.75, with the electric capillary number, $Ca_e = \epsilon_{ex}R_0E_0^2/\gamma$, standing for the ratio of the electric force and surface tension. The initial field strength $E_0 = (\psi_t - \psi_b)/N_z$ is increased from 0.2 to 1.0. In order to consider the effects of charge relaxation and charge convection, a finite $Re_e = 1$ is adopted. The droplet's deformation strength $Q = (L - D)/(L + D)$ is recorded, where L and D are the length and diameter of the droplet when it reaches a steady state. The LB simulation results are compared with both the simulations by Liu *et al.* (2019) and the theoretical formula proposed by Feng (2002). In figure 4(a), the results show that, for $R = 4.75$, the droplet exhibits oblate deformation. Both the simulations by Liu *et al.* (2019) and our current results align well with the theoretical prediction. For $R = 1.75$, the droplet shows prolate deformation, and our LB results are closer to Feng's (2002) theoretical prediction. It is noticeable that the simulations conducted by

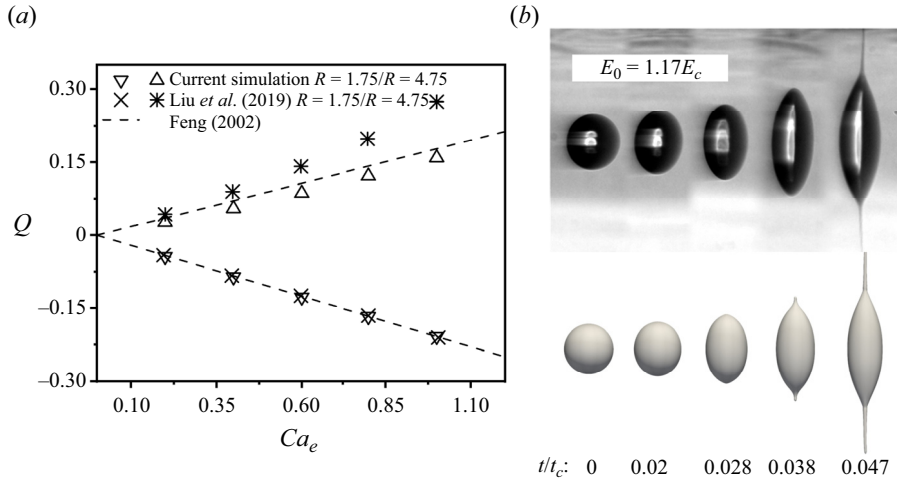


Figure 4. (a) Comparison of Q at steady state under different R and Ca_e with theoretical solutions and previous simulations. (b) Comparison between current simulation results (bottom) and previous experiment (Grimm & Beauchamp 2005) (top) for the Rayleigh fission of a methanol droplet in a strong electric field.

Liu *et al.* (2019) overestimate the droplet’s deformation strength, possibly due to their neglecting charge relaxation and charge convection effects in their simulations.

We then further extended our simulations to the more challenging three-dimensional two-phase EHD problem, where the LB model for the first time is used to simulate the Coulomb fission of a methanol droplet in a strong electric field. In this simulation, the density ratio of the methanol liquid and ambient gas is $\rho_{in}/\rho_{ex} = 1520$, $\mu_{in} = 0.032$ Pa s and viscosity ratio $\mu_{in}/\mu_{ex} = 320$, surface tension $\gamma = 0.0349$ N m⁻¹. The dielectric properties have $\epsilon_{in} = 12.2\epsilon_{ex} = 12.2\epsilon_v$, where $\epsilon_v = 8.854 \times 10^{-14}$ is the vacuum dielectric constant and $\sigma_{in} = 10^7\sigma_{ex} = 0.1$ S m⁻¹. The initial radius of the droplet is $R_0 = 10$ μ m. Similar to experiment (Grimm & Beauchamp 2005), the strength of the external electric field is set to a value greater than E_c , e.g. $E_0 = (\psi_t - \psi_b)/N_z = 1.17E_c$ for the target experiment, where the Taylor limit field strength is calculated as $E_c = \sqrt{4\gamma/(\sigma_{ex}R_0)}$. For our current simulation, the mesh resolution is $dx = R_0/60$ and time step is $dt = 7.5 \times 10^{-6}$ s. The simulation domain is a $N_x \times N_y \times N_z = 5R_0 \times 5R_0 \times 16R_0$ box. The comparison between simulation and experimental results (Grimm & Beauchamp 2005) is shown in figure 4(b), where an excellent agreement is found between our simulation and the experimental snapshots. Notably, the liquid filament at the tip of the droplet is successfully captured, with a radius approximately one order of magnitude smaller than R_0 as observed in experiments (Duft *et al.* 2003; Grimm & Beauchamp 2005; Cai *et al.* 2021).

At the end of this section, the mesh sensitivity analysis and charge conservation validation are conducted. In this test, the deformation of a methanol droplet at two different electric field intensities ($E_0 = 0.25E_c$ and $E_0 = 0.8E_c$) is simulated. The physical properties of the methanol droplet are consistent with the simulation parameters in figure 4(b), with the electrical conductivity ratios σ_{in}/σ_{ex} equals 10^7 . The grid resolution R_0/dx is increased from 30 to 60, with corresponding dx ranges from 0.15 to 0.3 μ m in physical units. The evolution of the aspect ratio (L/D) during the process is depicted in figure 5(a). The results indicate that, for the case with lower electric field intensities ($E_0 = 0.25E_c$), when R_0/dx is greater than 30, the grid resolution has little impact on

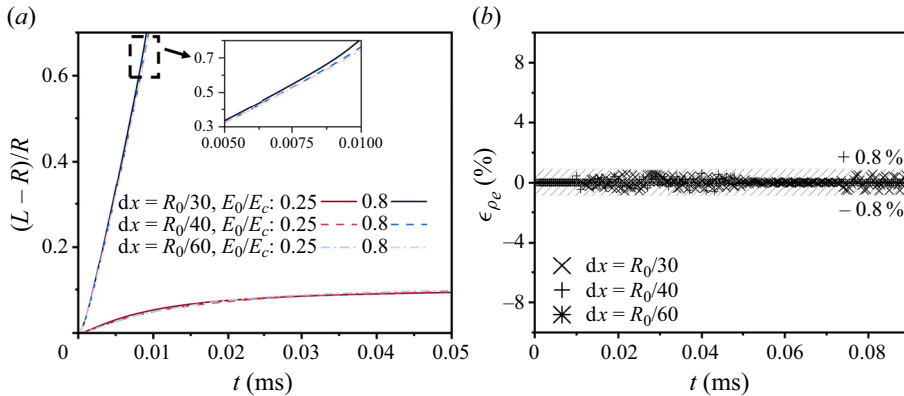


Figure 5. Time evolution of (a) aspect ratio of the droplet and (b) charge error under different grid resolutions.

	$\rho_{in}(\text{kg m}^{-3})$	$\mu_{in}(\text{Pa s})$	$\gamma(\text{N m}^{-1})$	$\varepsilon_{in}/\varepsilon_{ex}$	Γ_u
3-Ethyl. glyc.	1120	0.0454	0.0402	23.7	0.053
1-Octanol (1)	824	0.0089	0.024	10.34	0.21
1-Octanol (2)	824	0.0089	0.024	10.34	0.75
1-Butanol	800	0.00254	0.023	17.84	5.96
1-Propanol	803	0.00194	0.024	3.92	7.73
Methanol	795	0.00059	0.021	12.92	56.2

Table 2. Liquid properties of the electro spray simulation.

the simulation results. For the case with higher electric field intensities ($E_0 = 0.8E_c$), only minor differences were observed for the lowest resolution ($R_0/dx = 30$) in the final stage (as illustrated in the inset), during which the tip of the droplet begins to develop a liquid filament. The time evolution of the error in the total charge of the droplet during its deformation process is also recorded, where the error is calculated as $\epsilon_{\rho_e} = \sum \rho_e / \sum |\rho_e| \times 100\%$. Ideally, $\sum \rho_e$ should be kept as 0 when the conservation of charge is fully satisfied. As shown in figure 5(b), the charge error for the proposed LB model in this study is below 0.8%. For denser grids (i.e. $R_0/dx = 60$), this error is reduced to less than 0.1%.

3.4. Simulation of droplet electro spray

In this section, we simulate the electro spray of a suspended liquid droplet in an electric field and compare the ejected diameter with the scaling laws proposed by Gañán-Calvo *et al.* (2016). Table 2 summarizes the properties of the liquid droplets used in our simulations, where the governing dimensionless number Γ_u is $\Gamma_u = \delta_u^{5/3} (\varepsilon_{in}/\varepsilon_{ex})^{5/12}$, and the parameter δ_u is given as $\delta_u = [(\gamma^2 \rho_{in} \varepsilon_{ex}) / (\mu_{in}^3 \sigma_{in})]^{1/3}$ (Gañán-Calvo 1999). Six different cases with a wide range of Γ_u are simulated. Figure 6(a) illustrates the qualitative evolution of liquid droplets under three different values of Γ_u . It can be observed that, similar to the results obtained from experiments and simulations (Gañán-Calvo *et al.* 2016), the suspended droplets are elongated under the influence of electric field forces, forming a liquid jet and undergoing electro spraying. Moreover, consistent with

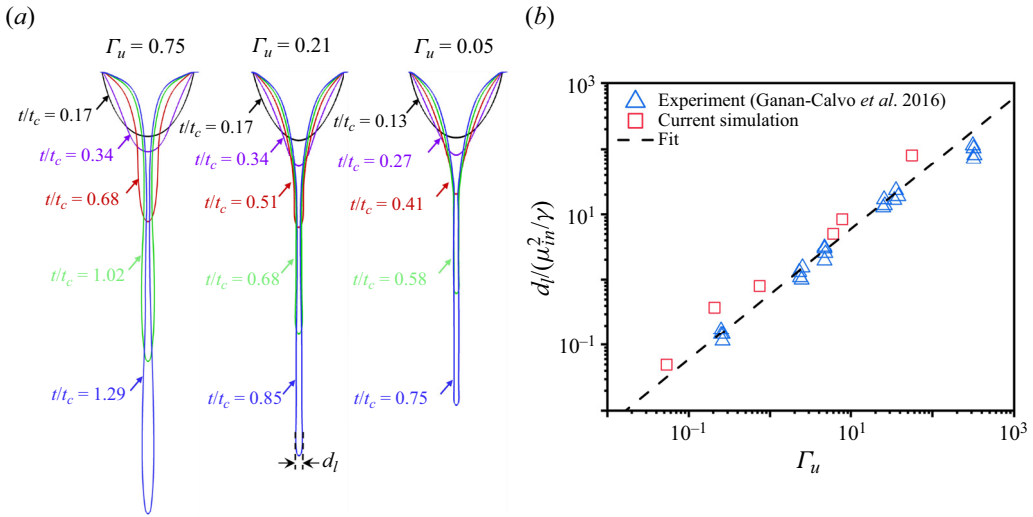


Figure 6. (a) Evolution of droplet profiles under different Γ_u . (b) Quantitative comparison of ejected droplet diameters with experimental results and linear fitting equation.

the qualitative findings from experiments (Gañán-Calvo *et al.* 2016), the diameter of the ejected droplet d_l from the jetting tip is increased with Γ_u . Furthermore, the ejection time and the length of the jet are also increased with Γ_u due to a slower charge relaxation.

Figure 6(b) presents a quantitative comparison between our LB simulation results of d_l and experimental results (Gañán-Calvo *et al.* 2016). The dashed line in the figure represents the linear fitted function $d_l = 0.6\Gamma_u(\mu_{in}^2/\gamma)$ (Gañán-Calvo *et al.* 2016). It can be observed that our simulation results are in line with the experimental data and the linear fitted function across a wide range of Γ_u . Besides, it is found that our LB simulation results exhibit good agreement with the simulation results and experimental data achieved by Gañán-Calvo *et al.* (2016). This is because both our EHD-LB model and their EHD-VOF model consider the effects of electric charge transport at the interface. On the other hand, the charge convection is considered in our simulations while it is ignored in the EHD-VOF model. Compared with the experimental results, our simulations slightly overestimated the size of d_l . In conclusion, the good agreement between our simulation results and experimental/theoretical results in the present validation test provides evidence that our proposed model can accurately simulate complex EHD phenomena.

4. Study of droplet equatorial streaming in an electric field

In this chapter, the validated LB model is employed to simulate the equatorial streaming of a droplet in an electric field. Firstly, it introduces the numerical set-up and simulation parameters. Then, it presents the morphologies of droplet equatorial streaming under different simulation conditions. Subsequently, a detailed analysis of the dynamic evolution of the droplet before its first breakup is conducted. Finally, the mechanisms of droplet breakup during equatorial streaming are discussed.

4.1. Problem description and numerical set-up

Figure 7 shows the simulation domain in Cartesian coordinates, with a droplet placed at the centre of a rectangular box. The initial radius of the liquid droplet is R_0 . The

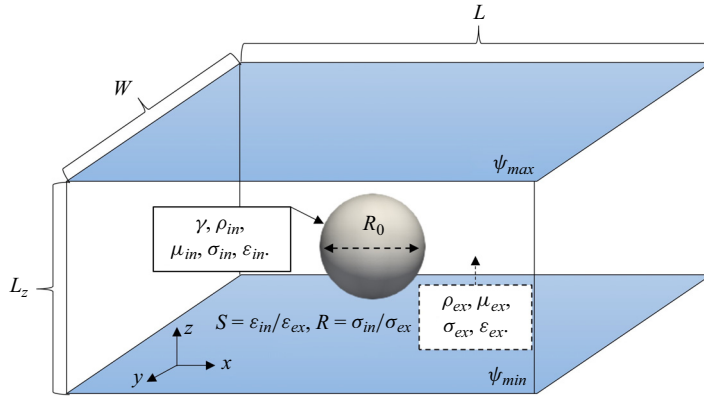


Figure 7. Schematic of the simulation domain.

dimensions of the simulation domain are set to a length (L) and width (W) of $9R_0$, with a height (L_z) of $5R_0$. The top and bottom walls are designated as no-slip boundaries and are assigned constant voltages. The voltage on the top surface is ψ_{max} , and on the bottom surface is ψ_{min} . The four lateral walls are set as periodic boundaries. γ , ρ_i , μ_i , ϵ_i and σ_i represent surface tension, density, viscosity, dielectric permittivity and electrical conductivity, respectively, where the subscript i is used to specify the external phase (ex) or the internal phase (in).

To reproduce the droplet equatorial streaming in an external electric field, following the experiment of Brosseau & Vlahovska (2017), the internal phase is set as low-viscosity silicone oil (SO) with low electrical conductivity ($\rho_{in} = 910 \text{ kg m}^{-3}$, $\mu_{in} = 0.0048 \text{ Pa s}$, $\epsilon_{in} = 3.2\epsilon_v$, $\sigma_{in} = 2 \times 10^{-12} \text{ S m}^{-1}$), while the external phase is set as high-viscosity castor oil with high electrical conductivity ($\rho_{ex} = 900 \text{ kg m}^{-3}$, $\mu_{ex} = 0.48 \text{ Pa s}$, $\epsilon_{ex} = 4.59\epsilon_v$ and σ_{ex} is varied correspondingly with the conductivity ratio $R = \sigma_{in}/\sigma_{ex}$). The surface tension and radius of the droplet are chosen as the same as the experiment, i.e. $\gamma = 0.0041 \text{ N m}^{-1}$ and $R_0 = 1 \text{ mm}$. The field strength of the external electric field is determined by the voltage contrast of the bottom wall and top wall, where $E_0 = (\psi_{max} - \psi_{min})/L_z$. It is worth noting that the conversion between lattice units and physical units requires selection of appropriate reference length and time scales. In the following simulations, the reference length $dx = R_0/50 = 20 \mu\text{m}$ and reference time $dt = 7.5 \times 10^{-6} \text{ s}$ were employed. It should also be noted that, for the current set-up, the total grid number of the simulation domain exceeds 50 million. Our code is parallelized by using MPI, and for a typical case (modelling the dynamic behaviours of the droplet for 1.1 s), the computational cost is approximately 4000 CPU running over 10 hours. All simulations are conducted on the United Kingdom national supercomputer Archer2.

This study aims to obtain a further understanding of droplet equatorial streaming. To this end, two governing parameters of the process are focused on: the electric field strength (E_0) and the conductivity contrast ($1/R$). In the existing studies for droplet equatorial streaming (Brosseau & Vlahovska 2017; Wagoner *et al.* 2020, 2021), details of droplet evolution at higher conductivity contrasts (i.e. $1/R > 2000$) remain unknown. Regarding the influence of electric field strength, it has not been systematically explored in previous experimental and simulation studies. For a droplet undergoing Coulomb fission, a necessary condition is that $E_0 > E_c = 6.35 \text{ KV cm}^{-1}$ (Gawande *et al.* 2017; Misra & Gamero-Castaño 2023). Besides, for the droplet equatorial streaming, the electrical

Lattice Boltzmann modelling

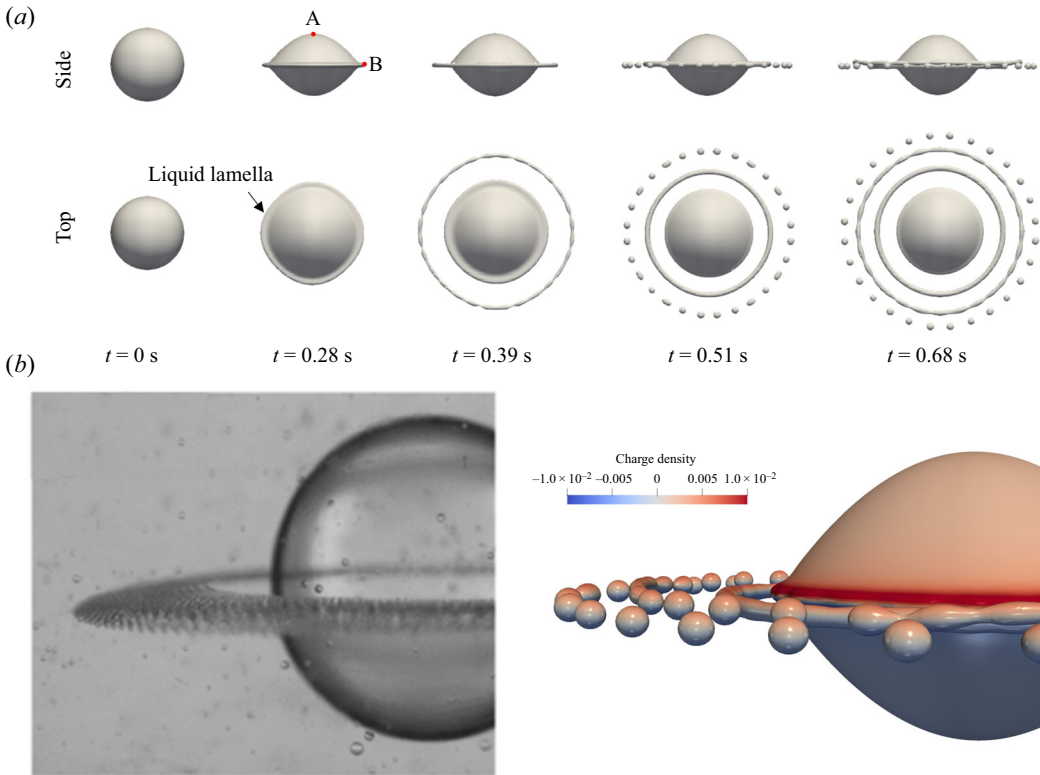


Figure 8. (a) Transient evolution of droplet equatorial streaming. (b) Experimental (Brosseau & Vlahovska 2017) (left snapshot) and simulation results (right snapshot) of the equatorial streaming for a droplet; simulation snapshot with the droplet surface coloured by charge density.

conductivity contrasts have $1/R \gg 1$ (Wagoner *et al.* 2020, 2021). Subsequently, for the following simulation, we change $1/R$ from 800 to 10 000, and E_0 is varied from $0.75E_c$ to $2.0E_c$, with the corresponding electric capillary number Ca_e ranging from 2.2 to 16.

4.2. Morphologies of droplet equatorial streaming

Figure 8(a) illustrates a typical process of a droplet equatorial streaming in an electric field, where $E_0 = 1.05E_c$ and $1/R = 2000$. The droplet is observed to gradually flatten under the effects of the electric field. A liquid lamella becomes noticeable at the equator of the mother droplet, because of the squeezing effect. As the droplet continues to deform, the liquid lamella forms a liquid ring and detaches from the equator. The detached ring continues to expand while an instability wave develops over it, eventually breaking into dispersed satellite droplets. During the process, new liquid rings continue to form from the equator of the mother droplet, undergoing expansion and breakage, thus constituting the equatorial streaming of the droplet. Figure 8(b) shows a qualitative comparison of the simulation snapshot with the experimental snapshot (Brosseau & Vlahovska 2017) for drop equatorial streaming. As can be seen, our simulation successfully reproduces the equatorial streaming phenomenon that when a droplet is subjected to an electric field, concentric fluid rings around the droplet are generated from the equator of the droplet, which finally break up to form hundreds of satellite droplets.

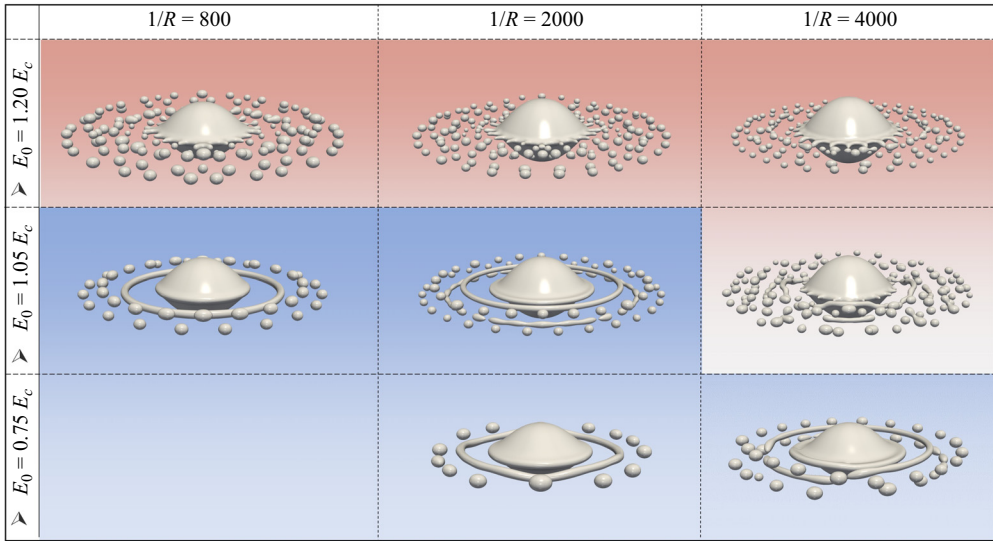


Figure 9. Snapshots of droplet equatorial streaming under different simulation parameters. Images in blue background represent ring equatorial streaming, and those in red background indicate fingering equatorial streaming.

Subsequently, we conducted simulations over a wider range of operation parameters, revealing two distinct break mechanisms behind the droplet equatorial streaming. Under conditions similar to the experimental conditions (Brosseau & Vlahovska 2017), i.e. lower E_0 and smaller $1/R$, the droplets displayed a liquid ring equatorial streaming process which is the same as the experimental results. However, for high E_0 and large $1/R$, the droplets exhibit a novel fingering equatorial streaming process. Figure 9 qualitatively illustrates the different break mechanisms of equatorial streaming under various conditions. Results with a blue background represent ring equatorial streaming of the droplets, while those with a red background depict fingering equatorial streaming. Unlike the ring equatorial streaming described in figure 8(a), for fingering equatorial streaming, multiple liquid fingers are generated at the equator of the mother droplet. Subsequent satellite droplets can be observed continuously detaching from these liquid fingering tips at the equator, as opposed to those being generated due to the continuous breakup of liquid rings. Supplementary movie 1 and movie 2 show the evolution of ring equatorial streaming ($1/R = 1500$, $E_0 = 1.05E_c$) and the fingering equatorial streaming ($1/R = 2000$, $E_0 = 1.50E_c$), respectively. Additionally, it is evident that the number and size of satellite droplets vary in mechanisms, which will be analysed quantitatively in the following text.

In figure 10, temporal evolutions of the generation and the breaking processes of the liquid rings/fingers at the equatorial plane of the droplet are presented, where the droplet surface is coloured by the magnitude of the external electric force. In the figure, the first three columns of contours on the left represent the first, second and third detachments of liquid rings, respectively. It can be found that the external electric field force is maximum near the equator of the mother droplet, where the squeezing of the electric field force leads to the elongation and fragmentation of the liquid lamella at the equator. For the cases of $E_0 = 1.05E_c$, it is observed that a larger $1/R$ (i.e. $1/R = 2000$) resulted in a quicker detachment and breakup of the liquid rings. Compared with the case with a smaller $1/R$ ($1/R = 800$), the satellite droplets generated were smaller in size but more plentiful in number. The breakup of the liquid rings via a classical capillary instability (which is also

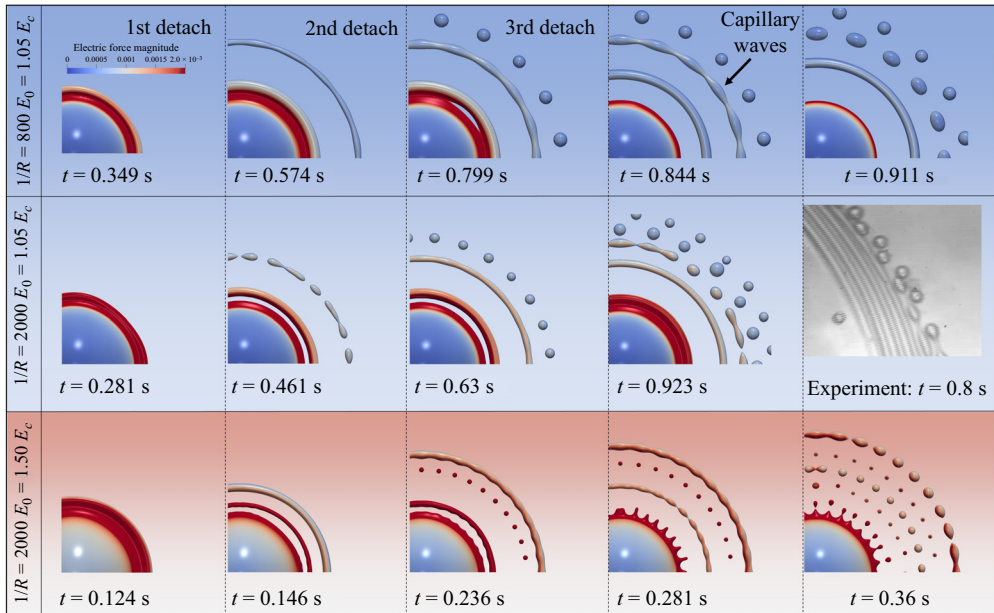


Figure 10. Dynamic evolution of localized magnification of droplet ring equatorial streaming (blue background) and fingering equatorial streaming (red background). The droplet surface is coloured by the electric field force magnitude. The inset figure (grey) represents the experiment (Brosseau & Vlahovska 2017) snapshot of droplet equatorial streaming.

known as Rayleigh Plateau instability) (Burton & Taborek 2011; Gawande *et al.* 2019), involves the continuous formation of necking and expansion along the circular direction. The experimental snapshot (grey inset) also confirmed this phenomenon. For the case of fingering equatorial streaming ($E_0 = 1.50E_c$ and $R = 1/2000$), its initial state is similar to ring equatorial streaming, where 2–3 liquid rings detach from the mother droplet and break into satellite droplets. In this case, it is observed that the first liquid ring is accompanied by a smaller daughter liquid ring, which is consistent with the experimental findings (Brosseau & Vlahovska 2017). Then, as the last ring detaches ($t = 0.236$ s), unstable liquid fingers develop at the edge of the mother droplet. These unstable liquid fingers are excited by instability waves in continuously detaching liquid rings. It can be evidenced that, with the detachment of the last ring, liquid fingers immediately form, and there is continuous contraction and expansion on the last detached ring (at $t = 0.281$ s). After the appearance of the liquid fingers, all subsequent satellite droplets are directly generated from the tip of the fingers, demonstrating an unstable mechanism distinct from the ring equatorial streaming. Regarding the diameter of the detached liquid rings, we observe that, in cases with relatively low electric field strength (i.e. $E_0 = 1.05E_c$), the diameters of the first three detached liquid rings are similar, with a diameter of approximately $d_r/d_0 \sim 0.04$. However, for cases with higher electric field strength (i.e. $E_0 = 1.5E_c$), the detachment of the first larger liquid ring $d_r/d_0 \sim 0.06$ is immediately followed by the detachment of a smaller ring $d_r/d_0 \sim 0.02$. Such occurrences of smaller sub-liquid ring detachment have also been observed in experiments (Brosseau & Vlahovska 2017). In the following § 4.3, we provide a detailed discussion and analysis of the sizes of detached liquid rings and satellite droplets.

As indicated in figures 8 and 10, compared with experimental results, the diameter of the liquid ring (d_r) is wider in our simulation results, and the gaps between the liquid

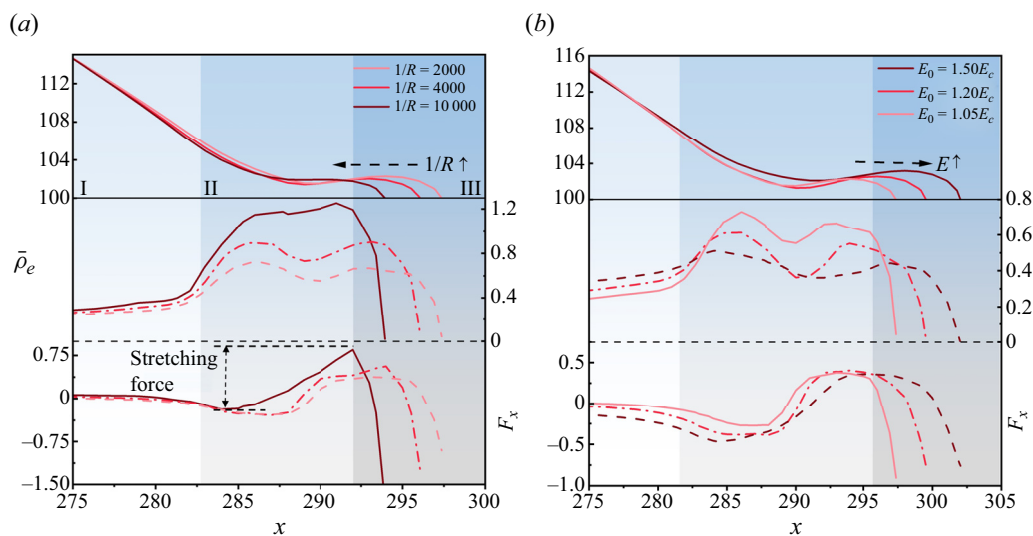


Figure 11. For cases with different (a) $1/R$ and (b) E_0 , at the critical moment before the first liquid ring detachment from the droplet, the profiles of the liquid lamella near the droplet equator (first row), the corresponding distribution of charge density (second row) and the corresponding electric field force in the direction of droplet expansion (third row).

rings are large (e.g. when $\mu_{in}/\mu_{ex} = 100$, $d_r/d_0 \sim 0.01$ for experiment, $d_r/d_0 \sim 0.04$ for our simulations). Several reasons may account for these discrepancies: (i) our simulation conditions may not perfectly match the experimental conditions, as the accurate value for $1/R$ was not provided in the original experimental results. (ii) In our simulations, the conductivity and dielectric permittivity at the interface are characterized by using log interpolation and linear interpolation. In reality, the distribution of electrical properties between the different phases is more complex. (iii) Limited by the computational resources, the interface thickness is set as $w/d_0 = 0.05$. This implies that the interface width is still of the order of micrometres. For real-world scenarios, the interface thickness is often in the nanometre range. Despite there being some quantitative differences between the simulation and experimental results, it is important to note that the model proposed in this paper qualitatively replicates the equatorial streaming process of a liquid droplet. Specifically, the model accurately captures, for the first time, the continuous detachment of the liquid rings from the equator and the subsequent splitting of the liquid rings into several hundred satellite droplets. Also, thanks to the quantitative results provided by numerical simulations, in the following study we reveal the power-law relation for the charge evolution during droplet equatorial streaming, propose a theoretical model for the evolution of the droplet radius and height and quantitatively investigate the breakup mechanism of the droplet. Moreover, by changing the operation conditions, our simulations revealed a new fingering equatorial streaming mechanism. These results are essential for studying the underlying physical mechanisms of droplet equatorial streaming.

To gain a better understanding of why different values of E_0 and $1/R$ lead to distinct instability mechanisms, we quantitatively analyse the profiles (first row), charge density ($\bar{\rho}_e$, second row) and lateral external electric force (F_{e-x} , third row, the ‘+’ and ‘-’ symbols represent the directions of liquid droplet expansion and contraction, respectively) near the liquid lamella at the equator before its first breakup under various $1/R$ (figure 11a) and E_0 (figure 11b). The droplet profile is divided into three different regions along the expansion direction (X -axis) based on the morphologies. Region I, situated near

the mother droplet, exhibited similar morphologies for various $1/R$, and with nearly uniform $F_{e,x}$, which is due to the fact that the mother droplet is mainly squeezed by the longitudinal external electric field force. For cases with different E_0 , this region also displayed consistent profiles, similar $\bar{\rho}_e$ and $F_{e,x}$. It is noteworthy that in cases with higher E_0 , $\bar{\rho}_e$ in this region is larger, which confirms Gauss's law (Melcher & Taylor 1969).

As for region II, corresponding to the neck position of the liquid lamella, the maximum value of $\bar{\rho}_e$ on the droplet's surface is observed at this location. This finding is distinct from the previous extensive modelling of perfectly dielectric droplets, where the maximum value of $\bar{\rho}_e$ appears at the droplet conical tips (Gawande *et al.* 2017, 2019; Sengupta *et al.* 2017). For equatorial streaming, it occurs at the neck of the equatorial liquid lamella, which is compatible with the theoretical findings for the finite conductivity model (Gawande *et al.* 2019; Misra & Gamero-Castaño 2023). Furthermore, it can be found that the maximum charge increased with $1/R$ and E_0 , which also aligns with Gauss's law. Regarding the magnitude of $F_{e,x}$, it initially increased in the direction of retraction ($-x$) and then increased in the direction of expansion ($+x$), which manifested as a stretching force (as marked in figure 11). It is this stretching force and its competition with surface tension that leads to the contraction of the liquid lamella in the longitudinal direction, forming the lamella neck. Quantitatively, it can be observed the stretching force increased with $1/R$ and E_0 . The qualitative results in figure 11 indicate that the appearance of the liquid fingers is caused by the destabilization of the liquid rings at the equator, before they are detached from the mother droplet. From the quantitative results in figure 11, it is proved that higher E_0 and $1/R$ result in greater stretching forces, implying a faster liquid ring departure velocity. Previous studies have found that the instability wave on the liquid ring is positively correlated with the expansion velocity of the liquid ring (Stone 1994; Zhao & Tao 2016). And in such cases, the breakup points are closer to the mother droplet. This explains why the phenomenon of equatorial streaming is observed with higher E_0 and $1/R$.

Region III represents the tip region of the liquid lamella, where $\bar{\rho}_e$ rapidly decreases from the maximum value to zero at the equatorial tip (point B in figure 8). The value of $F_{e,x}$ in the droplet's expansion direction initially decreases to zero and then increases in the direction of retraction. Considering that $\bar{\rho}_e$ is zero at this point, the electric field force here is solely contributed by the dielectric force. Therefore, from figure 11, it can be observed that $F_{e,x}$ at the equatorial tip increases with $1/R$ and is almost independent of E_0 . This finding is consistent with (2.7). For the maximum spreading diameter of the droplet before breakup, it is found that it decreased with increasing $1/R$, whereas it increased with increasing E_0 .

In this subsection, the equatorial streaming of a liquid droplet under different $1/R$ and E_0 is qualitatively demonstrated, revealing two distinct morphologies: ring equatorial streaming and fingering equatorial streaming. A qualitative overview of the detachment of the liquid lamella at the equator, the formation of the liquid rings/liquid fingers and the generation of satellite droplets is provided. Subsequently, quantitative analysis of the charge distribution and external electric force on the liquid lamella are employed to explain the generation of fingering equatorial streaming. The following subsection will focus on the dynamic behaviours of the droplet before it breaks, with emphasis on quantitatively studying critical parameters such as the droplet's total charge, spreading diameter and droplet breakup time.

4.3. Dynamic behaviours of the droplet

In the study of the EDH phenomenon, a critical point is understanding the behaviours of the charge density (Fernández de la Mora 2007; Vlahovska 2019), especially its

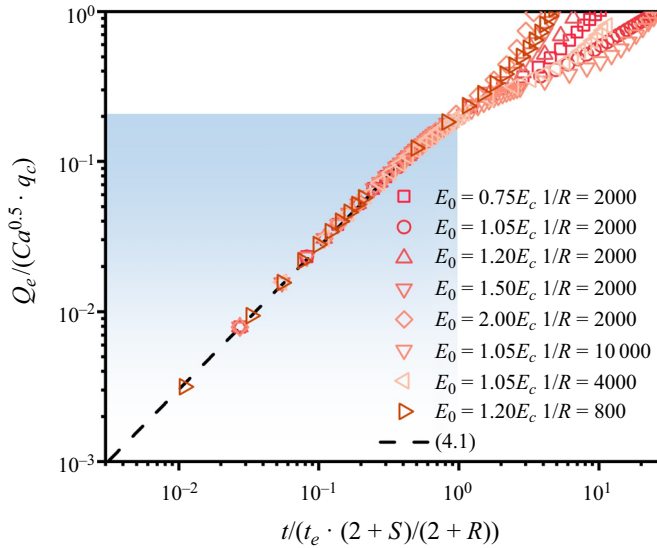


Figure 12. Evolution of the total charge carried by the droplet before the first liquid ring detachment, under different simulation conditions. The region dominated by charge relaxation is indicated by the blue background.

dynamic evolution over time and the charge carried by satellite droplets. This is of paramount importance for applications such as mass spectrometry analysis, separations, powder synthesis and others (Fenn *et al.* 1989; Ptasinski & Kerkhof 1992; Harris, Scott & Byers 1993). After applying an electric field, the charge equilibrium is disrupted. Positive and negative charges at the phase interface are driven towards the positive and negative ends closer to the electrodes under the influence of Coulomb forces (Fernández de la Mora 2007; Luo *et al.* 2020). In all cases, due to charge conservation, the total charge always equals 0. Therefore, $Q_e = \sum |\rho_e|$ is used to represent the total charge carried by the droplet. To explore the mechanism of charge evolution under different simulation parameters, the time is normalized by introducing a charge relaxation time that takes into account differences in electrical conductivity and dielectric coefficients (i.e. $t_e^{\sim} = t_e(2 + S)/(2 + R)$) (Brosseau & Vlahovska 2017). Regarding Q_e , it is normalized by using $Ca_e^{0.5} q_c$, where q_c is the Rayleigh charge limitation $q_c = 8\pi\sqrt{\gamma\epsilon_{ex}R_0^3}$.

The evolutions of the total charge of the droplet before the first ring detaching for different $1/R$ and E_0 cases are plotted in figure 12 with a logarithmic scale. It can be observed that, for all cases when $t/t_e^{\sim} < 1$ (blue background), the evolution of the total charge follows a power-law increase, with its evolution being fitted as

$$\frac{Q_e}{Ca_e^{0.5} q_c} = 0.25 \left(\frac{t}{t_e^{\sim}} \right)^{0.95}. \quad (4.1)$$

This result confirms the findings of Sengupta *et al.* (2017), who also found a power-law increase for the surface charge. The consistency exhibited by the total charge in this region is due to the fact that the evolution of the charge is dominated by the charge relaxation. Dividing time and total charge by t_e^{\sim} and $Ca_e^{0.5} q_c$, the influence of the charge relaxation can be normalized appropriately. Outside this region, the charge evolution varies from case to case. Specifically, the total charge increases faster under conditions of higher E_0 and lower $1/R$. As pointed out by Sengupta *et al.* (2017), within this region, the influence

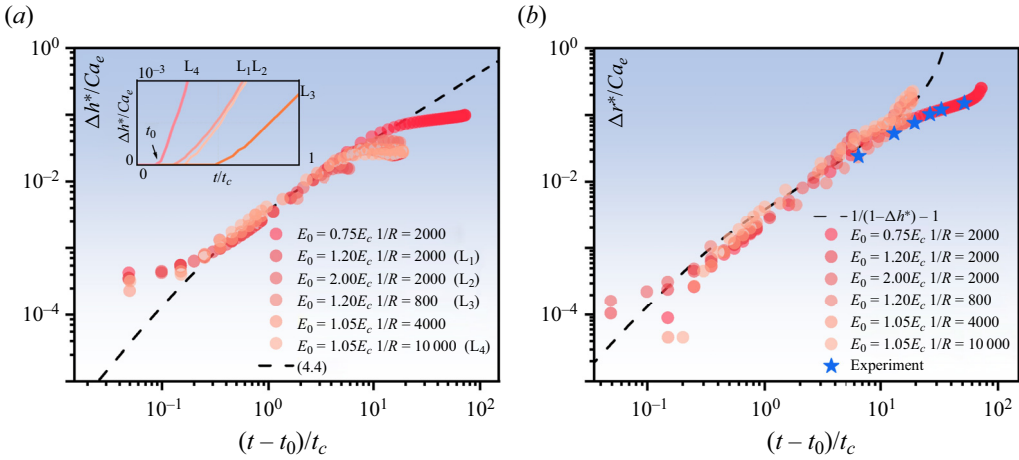


Figure 13. Under different simulation conditions, the time evolution of deformation magnitude in (a) height and (b) radius of the droplet before the first liquid ring detachment.

of charge convection cannot be neglected, particularly for cases with larger Reynolds numbers (Re_e). Considering Re_e increases with E_0 but decreases with $1/R$, our simulation results corroborate with the prediction from Sengupta *et al.* (2017).

Next, the evolution of the droplet’s height (H) and radius (R) before the first detachment of the liquid ring is investigated. Figures 13(a) and 13(b) indicate the time evolution of the droplet deformation magnitude in radius ($\Delta r^* = (R(t) - R_0)/R_0$) and height ($\Delta h^* = (R_0 - H(t))/R_0$) under various $1/R$ and E_0 , respectively. In the figure, Δr^* and Δh^* are generalized by using Ca_e and time t is normalized by capillary time $t_c = (R_0^3 \rho_{ex} / \gamma)^{0.5}$. The inset figure in figure 13(a) represents the initial state of droplet motion, it can be found that the droplet remains stationary for a very short period ($t_0, t_0 \ll t_c$) after applying the electric field. This very short stationary time is directly proportional to the charge relaxation time. Considering the charge relaxation time decreases when $1/R$ is increased, \tilde{t}_e (10 000) is used as a reference value (standing for the \tilde{t}_e when $1/R = 10\ 000$), the dynamic stationary time is given as $t_0 = 0.5(\tilde{t}_e (1/R) - \tilde{t}_e (10\ 000))$.

In figure 13, all the normalized results can be collapsed into one line. In this work, a new theoretical model is proposed to describe the transient evolution of the droplet height and radius. First, let us consider the transient evolution of the droplet in the direction of the electric field. To facilitate the analysis, we only consider forces on the symmetry plane of the droplet, i.e. on the x - z plane. When subjected to an electric field, the poles of the droplet (point A in figure 8) are subjected to a capillary force ($F_c \sim 2\gamma/H$), viscous force ($F_v \sim \mu_0/R_0 \Delta H'$) and electric field force ($F_e \sim \epsilon_0 E_0^2$). According to Newton’s second law, we can determine

$$m^* \frac{d^2(\Delta h^* R_0)}{dt^2} \sim \epsilon_0 E_0^2 - \frac{2\gamma}{R_0(1 - \Delta h^*)} - \frac{\mu_{ex}}{R_0} \times \frac{d(\Delta h^* R_0)}{dt}, \quad (4.2)$$

where m^* is the effective mass, with a dimension of $\text{kg m}^{-2} \sim \rho_{ex} R_0$ in this two-dimensional analysis. By non-dimensionalizing the above equations with $t^* = (t - t_0)/t_c$

$$\frac{d^2 \Delta h^*}{dt^{*2}} \sim Ca_e - \frac{2}{(1 - \Delta h^*)} - Oh \frac{d\Delta h^*}{dt^*}. \quad (4.3)$$

The Ohnesorge number $Oh = \mu_{ex}/\sqrt{2\gamma\rho_{ex}R_0} = 7.9$ is kept consistent for all cases. This non-dimensional number measures the ratio of viscous forces to surface tension and inertial forces. For the case of $Oh > 1$, the viscous force is dominant. Considering the surface tension of the simulated SO droplet is relatively small, for the initial stage of droplet motion, deformation is primarily governed by the competition between electric field forces and viscous forces. Therefore, we neglect the term related to surface tension. By incorporating the initial conditions $d\Delta h^*/dt^* = 0$ and $\Delta h^* = 0$ when $t^* = 0$, the above differential equation has the general solution

$$\Delta h^* = \alpha \left\{ \frac{Ca_e}{Oh}(t - t_0)/t_c + \frac{Ca_e}{(Oh)^2}(e^{-Oh(t-t_0)/t_c} - 1) \right\}, \quad (4.4)$$

where α is the fitting constant representing the weight ratio of electric field force and viscous force contributions. In this study, the best fitted α is 0.034. Additionally, considering that Oh is a constant, the above theoretical model is conserved with $\Delta h^*/Ca_e$, explaining why all simulated results can be collapsed into a line. It can be observed that the exponential term on the right-hand side of the model is similar to the dynamic evolution equation proposed before (Esmaeeli & Sharifi 2011; Mandal, Chaudhury & Chakraborty 2014), which describes the deformation of droplets under relatively small electric field strengths, primarily considering the effect of electric field force while neglecting viscous forces. Therefore, the equation proposed in this paper can be considered as an extended form of the previous models. In the context of the dynamic evolution of droplets in the lateral (radius) dimension, we assume that the droplet consistently takes on an elliptical shape throughout its morphological changes, with the conservation of its area. Hence, $\Delta r^* = 1/(1 - \Delta h^*) - 1$.

Our proposed models are depicted as dashed lines in figure 13. As shown in figure 13(a), the presented model aligns well with our simulation results. However, differences appear during the initial stage of droplet evolution ($t^* < 0.1$) and the terminal stage ($t^* > 10$). This discrepancy arises from the significant influence of the droplet's initial stationary period (t_0) on the results during the early stages. During this stage, the linear relationship for t_0 may not represent the actual situation. As for the terminal stage, the contribution of surface tension becomes non-negligible. As r^* is directly derived from h^* , in figure 13(b), it is found that there are also discrepancies between the proposed model and the simulation results at these stages. Nevertheless, during the dynamic evolution stage of the droplet ($t^* \sim 0.1-10$), the theoretical model and numerical simulation results are in excellent agreement. Notably, for our proposed model, the time and deformation magnitude that match the simulation results can span several orders of magnitude, especially considering the broad range of simulation parameters used in this study.

Next, it focuses on the critical moment before the first liquid ring is divided from the droplet. Firstly, our attention is on the total charge carried by the droplet at the critical moment. In 1882, Lord Rayleigh first predicted that a charged droplet would be unstable when its charge exceeded q_c (Rayleigh 1882; Duft *et al.* 2003). Over the subsequent centuries, a substantial amount of research has been dedicated to validating this prediction. A general consensus is that, when Q_e exceeds q_c or E_0 is greater than E_c , the droplet undergoes prolate fission. The droplet's poles will eject charged satellite droplets from both ends and the droplet will lose charge, typically around 15% to 50% of the total charge (Fernández de la Mora 2007). On the other hand, limited studies have been conducted to investigate the droplet's charge during its oblate fission. Figure 14(a) shows the total charge carried by the droplet before its first breakup (Q_c) and the total charge carried by the first liquid ring (Q_{ring}) for all the simulated cases in this work. Here, $Ca_e R/S$ for the X axis is

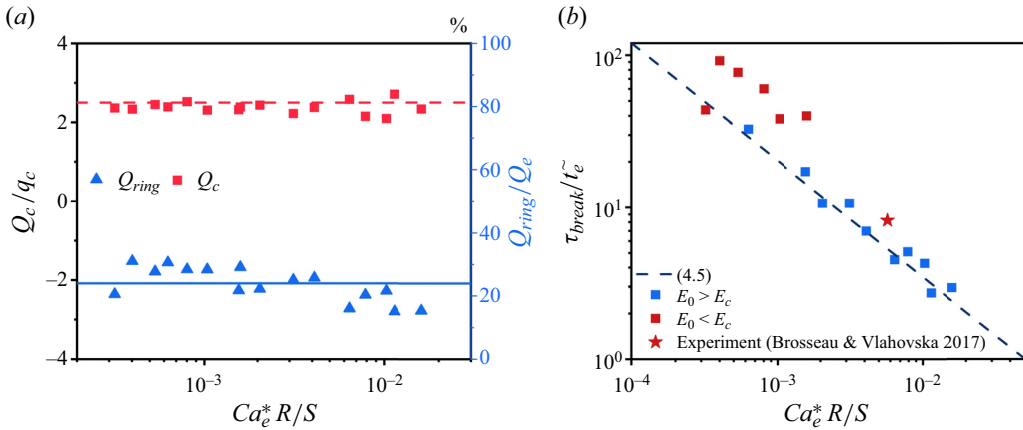


Figure 14. For all simulation cases in this study, (a) the total charge of the droplet Q_e at the critical moment of the first liquid ring detachment (red symbols, left Y-axis) and the proportion of the total charge carried by the detached liquid ring Q_{ring} (blue symbols, right Y-axis) and (b) the power-law decay relationship between the time of the first liquid ring detachment and $Ca_e R/S$.

used to distinguish between different simulation parameters. It can be observed that, for all cases, Q_e/q_c is approximately 2.5 (dashed line). It should be noticed that the charge loss by liquid ring streaming is approximately 24% of the total charge (solid line) for the first liquid ring detachment. In all cases, the charge loss is between 15% and 30% of the total charge.

In addition to the droplet charge, the critical time at which the first liquid ring breaks away from the droplet (τ_{break}) is also recorded, which is normalized by \tilde{t}_e and plotted in relation to $Ca_e R/S$ in figure 14(b). Here, Ca_e stands for the electric field strength, and ρ_e is increased with the electrical conductivity difference, as indicated by Gauss's law. Therefore, $Ca_e R/S$ can be regarded as the contribution of the Coulomb field forces under different E_0 and $1/R$. Interestingly, it can be found that, for the cases $E_0 > E_c$, the normalized τ_{break} exhibits a power-law decay relationship with \tilde{t}_e , where

$$\frac{\tau_{break}}{\tilde{t}_e} = 0.1 \left(\frac{Ca_e R}{S} \right)^{-0.77} \quad (4.5)$$

The experimental result by Brosseau & Vlahovska (2017) is also plotted on the same graph. The results indicate that the experimental breakup time aligns well with the exponential decay function found in this study. Nevertheless, it can be found that the results for cases of $E_0 < E_c$ deviate from the other cases.

To explore the underlying mechanisms of τ_{break} derivation for the $E_0 < E_c$ cases, the evolution of Q_e for the cases with $E_0 = 1.05E_c$ and $E_0 = 0.75E_c$ and different $1/R$ is plotted in figure 15. The total charge and time are non-dimensionalized by q_c and theoretical critical time (τ_{break_theory}) in (4.5), respectively. Additionally, the evolution curves are coloured based on the deviation of the droplet's radius per unit time ($\delta r^*/\delta t$); the critical moments when the droplet first experiences the liquid ring detachment are marked with a pentagram symbol on the graph. From the graph, it is evident that, for $E_0 > E_c$, the radius ($\delta r^*/\delta t > 0$) and Q_e steadily increase during the evolution, and the breakup point and critical Q_e are close to the theoretical values introduced above ($\tau/\tau_{break_theory} \sim 1$ and $Q_e/q_c \sim 2.5$). In the case of $E_0 < E_c$, it can be observed that there is a rapid initial increase in Q_e , followed by a slower rate of increase. During this period, the increase

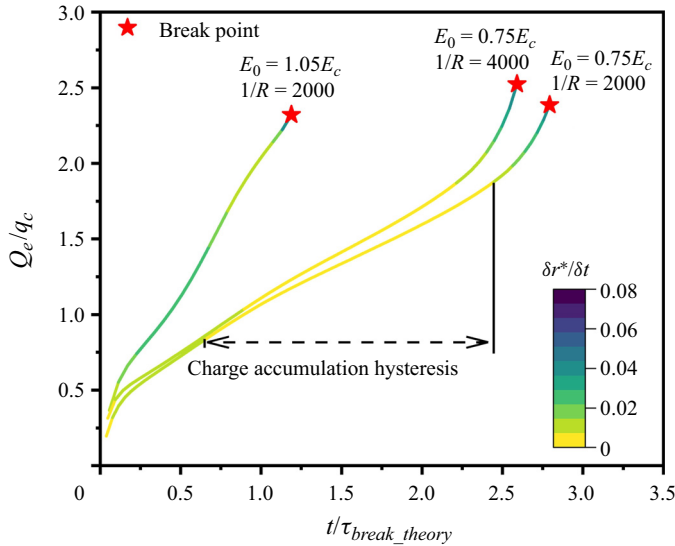


Figure 15. Charge accumulation hysteresis before the first liquid ring detachment. The evolution curve of charges over time is coloured by the increment of droplet radius per unit time ($\delta r^*/\delta t$).

in radius is approximately zero, indicating that the droplet is in a quasi-stationary state ($\delta r^*/\delta t \sim 0$). With the accumulation of charge, when $Q_e/(Ca_e^{0.5} q_c) > 1.5$, the droplet's radius begins to expand, and after this point, the charge also starts to accelerate its increase. We refer to the period of charge accumulation with the droplet in a quasi-stationary state as 'charge accumulation hysteresis'. Previous experimental (Luo *et al.* 2017; Abbasi *et al.* 2019) and numerical (Wagoner *et al.* 2020) studies also observed similar 'hysteresis' dynamics for droplet prolate fission. It is the presence of this hysteresis process that leads to longer breakup times for $E_0 < E_c$ and larger breakup charges compared with cases where $E_0 > E_c$.

In this section, a systematic study of the dynamic behaviours of droplets before the first liquid ring detachment is conducted. Firstly, it is found that there is a power-law relationship for the total charge over time. Secondly, a new theoretical model is developed to describe the time evolution of the droplet's radius and height. Finally, the critical moment of the first liquid ring detachment is emphasized. The droplet total charge, the charge carried by the liquid ring and droplet breakup time are quantitatively explored. In the following section, we will focus on the behaviours of the droplet after the breakup, including the distribution of satellite droplets, and instabilities occurring on the liquid ring and liquid fingers.

4.4. Breakup mechanisms of droplet equatorial streaming

From the quantitative results in §4.2, it is clear that, in all simulation cases, a liquid ring is first formed at the equator of the droplet during the onset of droplet equatorial streaming. This is followed by the breakup of the liquid ring into satellite droplets. To further investigate the breakup mechanism in droplet equatorial streaming, we focus on the breakup of individual liquid rings. Figure 16 first qualitatively presents the shapes of the liquid rings at the critical moments before the break with varying $1/R$ and E_0 (highlighted in different colours). Here, clear axisymmetric perturbation is observed, which is referred to as varicose instability (Rayleigh 1878). To further investigate this

Lattice Boltzmann modelling

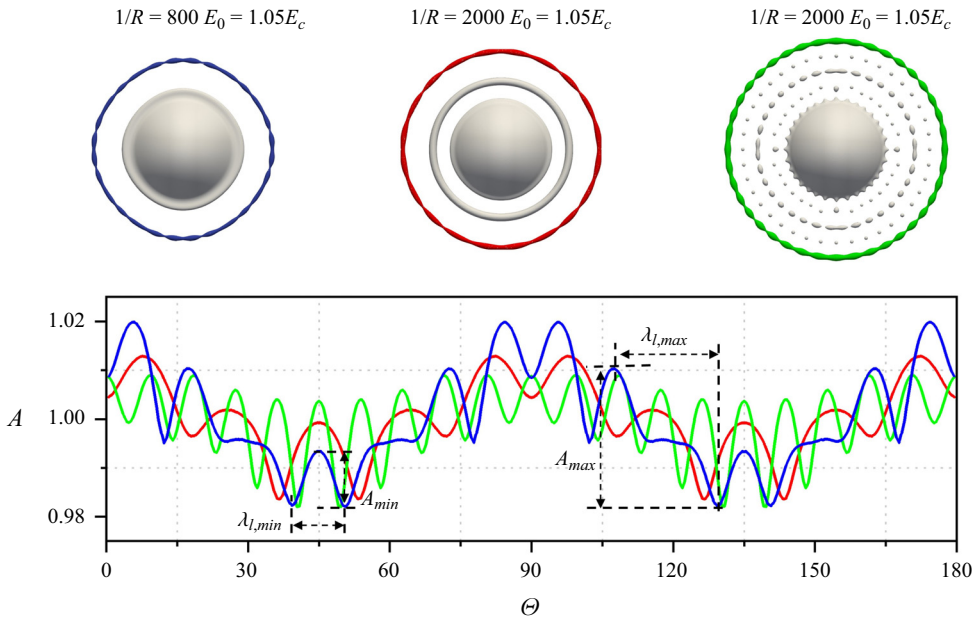


Figure 16. Snapshots of the streaming droplet at the critical moment just before the first liquid ring (highlighted) breakup, along with a quantitative diagram of the unstable waves at the edge of the liquid ring.

instability phenomenon, the instability waves at the edges of the rings are quantitatively plotted in figure 16. Different colours correspond to different cases, where the amplitude (A) is normalized by the mean distance to the droplet centre, and θ represents the angle with respect to the central axis. Due to symmetry, only the results for the right half of the droplet are shown.

By pairing the quantitative and qualitative results in figure 16, it can be observed that the peaks of the instability waves represent the bulges at the edges of the liquid ring. Meanwhile, the troughs correspond to the constriction or neck of the liquid ring, which is often the location where the breakup occurs. For the cases with the same E_0 , the smaller $1/R$ brings the larger wave amplitude. Comparing the ratio of maximum/minimum wavelength ($\lambda_{l,max}/\lambda_{l,min}$) and maximum/minimum amplitude ($A_{l,max}/A_{l,min}$) (as indicated in figure 16) for different $1/R$ cases, it can be found that the difference between the wavelength and amplitude becomes more pronounced for smaller $1/R$, which corresponds to a more extensive distribution of satellite droplet sizes and relatively larger satellite droplets. This prediction can be confirmed by figure 10. For the same $1/R$ but different E_0 cases, a larger E_0 leads to a shorter wavelength, resulting in a denser population of satellite droplets. Also, for the larger E_0 case, the wavelengths and amplitudes are relatively consistent between different peaks, implying uniform satellite droplet diameters. This can be supported by the qualitative results of the liquid ring after fragmentation in figure 10.

Subsequently, the critical wavelength (λ_l), the average radius of the liquid ring (r_l) and the mass of the liquid ring (m_l) at the critical moment before the rings break are recorded. The recorded results for different $1/R$ and E_0 are provided in table 3. A consistent $r_l/R_0 \sim 4\%$ in all cases is observed, in agreement with linear instability theory and experiment findings where $r_l \sim (\mu_{in}/\mu_{ex})^{0.5}$ (Stone 1994). We observed that the mass of the first detaching liquid ring increases with the increase of $1/R$ and E_0 , with the ratio of mass loss

$1/R$	E_0/E_C	λ_l/R_0	m_l/M_0	r_l/R_0	λ_l/r_l	t_l/t_c
10 000	1.05	0.31	0.013	0.043	7.21	6.04
4000	1.05	0.33	0.016	0.044	7.62	9.01
2000	1.05	0.43	0.022	0.044	9.73	11.33
1500	1.05	0.57	0.026	0.048	11.91	13.60
800	1.05	0.71	0.040	0.042	16.78	15.8
2000	1.20	0.41	0.029	0.042	9.51	8.32
2000	1.50	0.39	0.047	0.046	8.65	2.21

Table 3. Under different simulation conditions, before the first liquid ring breakup, the wavelength of the edge unstable wave (λ_l), the average radius (r_l) and mass (m_l) of the first liquid ring and the average interval of liquid ring detachment (t_l).

from the mother droplet (m_l/M_0) increasing from approximately 1.5% to 5%. Regarding λ_l , we note a decrease with an increase in $1/R$ and E_0 , consistent with the aforementioned findings. It is noteworthy that the critical wavelength exhibits an exponential decay as $\lambda_l \sim 2\pi + \exp(1/R)$ and tends to a convergent value $\lambda_l/r_l \sim 2\pi$ when electrical insulation state (i.e. $\sigma_{ex} = 0$), closely adhering to the classical Taylor theory (Tomotika 1935). This outcome serves as further evidence that the fragmentation of the liquid ring is primarily governed by capillary instability.

Meanwhile, the average intervals of liquid ring detachment (t_l) are recorded. As indicated in the table, the frequency of liquid ring detachment increases with the increase of $1/R$ and E_0 . Especially at a large E_0 , it can be observed that a smaller daughter ring (with a radius of $\sim 0.1r_l$) closely follows the detachment of the first liquid ring (as shown in figure 10). Similar phenomena have also been observed in previous experiments (Brosseau & Vlahovska 2017). Ultimately, with the fragmentation of this secondary liquid ring, smaller daughter droplets form around the primary satellite droplet. As analysed in § 4.2, the occurrence of liquid fingers for higher $1/R$ and E_0 cases are attributed to the excitation by unstable waves on the liquid ring. Therefore, the results in table 3 corroborate this observation, as λ_l and t_l decrease with the increase of $1/R$ and E_0 .

Variations in the unstable wavelength for different $1/R$ directly result in noticeable differences in the size distributions of the fragmented droplets produced. In figure 17, a statistical analysis of the size distribution ($d \ll d_0$) of satellite droplets after the breakup of the first two concentric liquid rings under different $1/R$ is presented. Simultaneously, we illustrate the corresponding qualitative results with the highlighted blue regions representing the measured satellite droplets. Following the prediction of the fragmentation–fusion scenario, the satellite droplet size distribution can be fitted by using gamma functions (Villermaux, Marmottant & Duplat 2004; Kooij *et al.* 2019). Notably, for larger values of $1/R$, the average size of the corresponding satellite droplets is smaller. In contrast, for smaller $1/R$, the size distribution is wider and the average size is larger. It is observed that, as $1/R$ increases from 800 to 10 000, both the average size and the size distribution range of the satellite droplets approximately doubled, with the number of satellite droplets increasing by approximately 50%. This observed droplet size distribution aligns with the aforementioned analysis of liquid ring instability.

As the liquid ring continuously detaches and breaks over time, the outcome due to droplet equatorial streaming is the generation of hundreds of dispersed satellite droplets on the equatorial plane of the droplet. The terminal size distribution of satellite droplets under different simulation parameters is plotted in figure 18. Since we have previously established that the size distribution of satellite droplets follows a gamma distribution, the

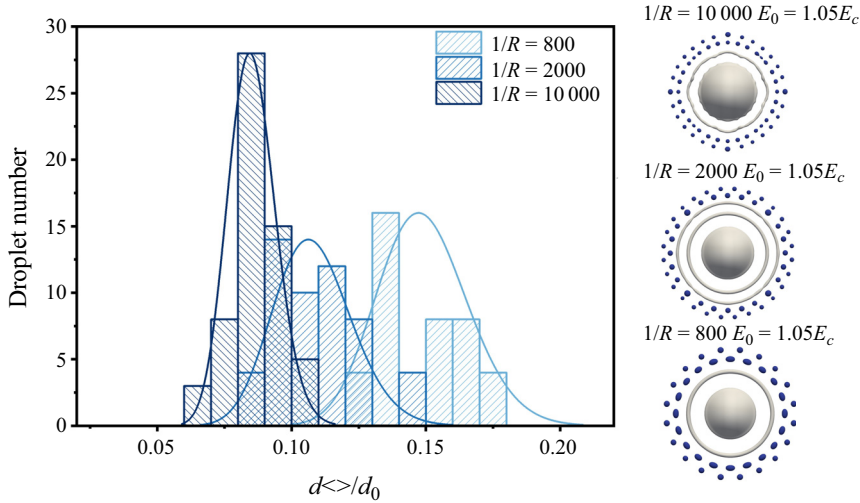


Figure 17. For cases with different $1/R$, the satellite droplet size distribution after the breakup of the first two liquid rings, along with the qualitative comparison. The solid line represents the gamma function fit of the satellite droplet size distribution.

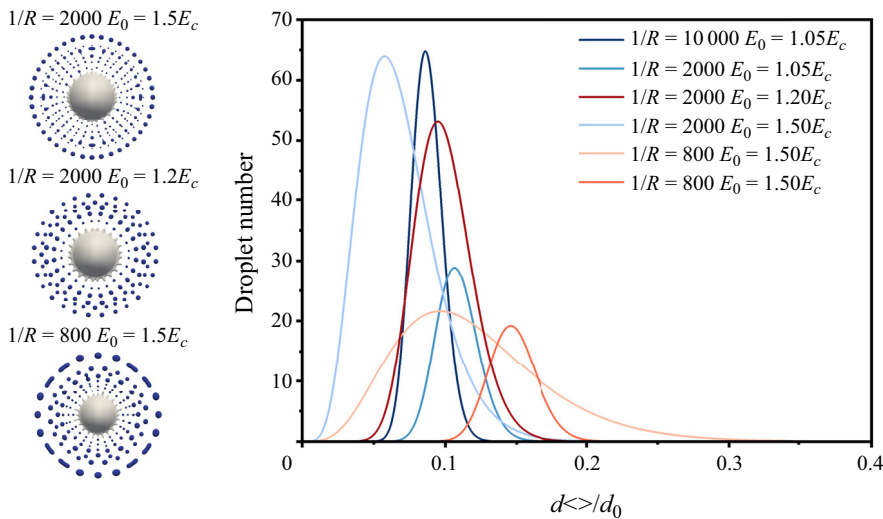


Figure 18. Size distribution of satellite droplets produced by droplet equatorial streaming under different simulation conditions, directly displayed by their best-fitted gamma functions. The corresponding qualitative results in the figure are satellite droplets produced by fingering equatorial streaming.

results are directly displayed through best-fitted gamma functions. From the graph, it is evident that, consistent with the size of satellite droplets from the liquid rings, the average radius of the final satellite droplets and their size range decrease with an increase in $1/R$. The average size and size distribution range of satellite droplets are similar to the results in figure 17 for cases with $E_0 = 1.05$, the total number of satellite droplets for the case of $1/R = 10000$ is approximately 125 % higher than the case with $1/R = 800$. For a given $1/R$, similar to the outcomes of a single liquid ring breakup, we observe a reduction in the

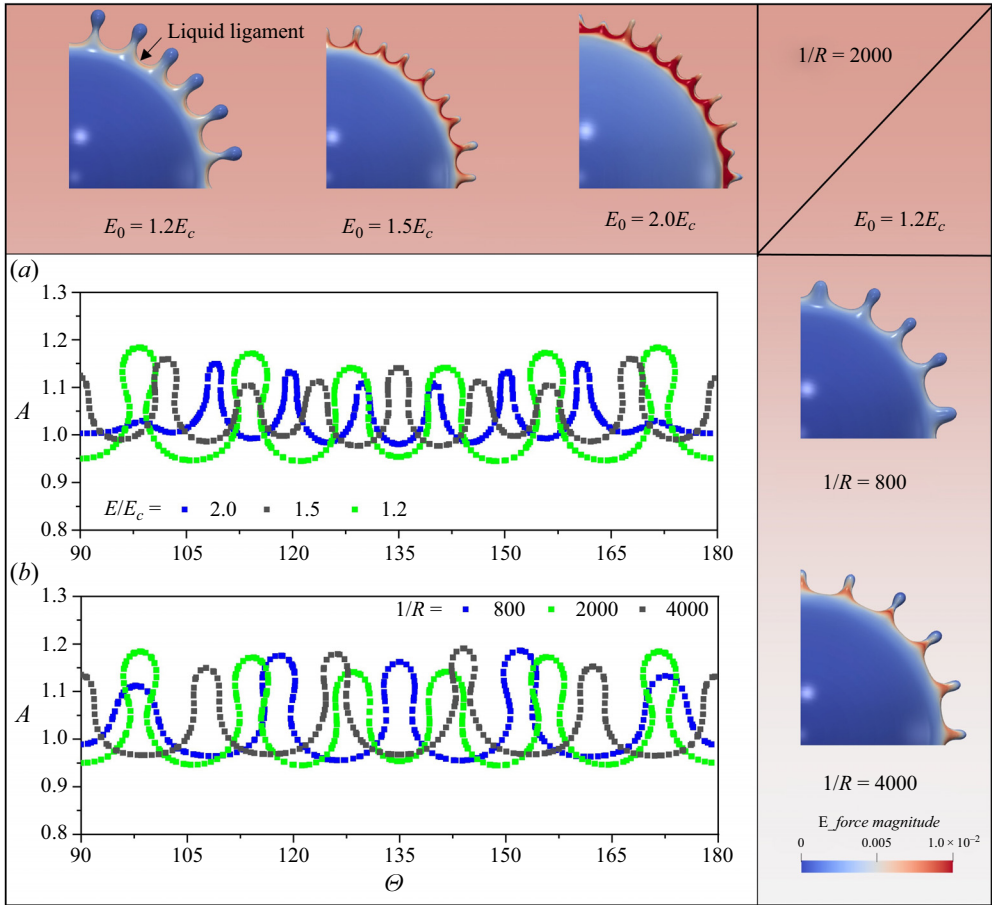


Figure 19. For fingering streaming, quantitative schematics of liquid fingers around the mother droplet under different (a) E_0 and (b) $1/R$, along with corresponding snapshot results from simulations.

average radius of satellite droplets with an increase in E_0 . The observed minimum satellite droplets have diameters $d_{(min)}/d_0 = 30$, corresponding $30\ \mu\text{m}$ in physical unit.

Nevertheless, different from the case of single liquid ring fragmentation, the size distribution of satellite droplets broadens with an increase in E_0 . This anomalous result in the distribution of satellite droplets is attributed to the occurrence of smaller daughter droplets around the satellite droplets for larger E_0 . It is crucial to note that, in addition to the liquid ring breakup, finger breakup also occurs for cases with larger E_0 . As indicated in the qualitative snapshots in figure 18, satellite droplets produced by liquid fingers (closer to the centre) are notably smaller than those generated by liquid ring breakup (outermost satellite droplets). Due to the multiple influences of the uneven wavelength on the liquid ring, daughter rings and fingering breakup, we observe the broadest size distribution for the case of $1/R = 800$ with $E_0 = 1.5E_c$.

As indicated by the above results, fingering equatorial streaming directly leads to the generation of satellite droplets with sizes distinct from those resulting from liquid ring rupture. To get a deeper understanding of the phenomenon of fingering equatorial streaming, in figure 19, snapshots of the liquid fingers (also called liquid filaments) at the edge of the mother droplet under different E_0 (vertical columns) and $1/R$ (horizontal

rows) are extracted, at the instant before the first ejection of satellite droplets; the droplet is coloured by the total electric force. The liquid fingers form at the edge of the mother droplet immediately after the detachment of 2 to 3 liquid rings. Similar to [figure 16](#), we quantified the corresponding edge profiles in (a) with different E_0 and (b) with different $1/R$, facilitating a more intuitive presentation of the wavelength and radius of liquid fingers. From a qualitative perspective, it can be found that the ejection of satellite droplets from the liquid finger is mainly controlled by the mechanism of end pinching ([Wang et al. 2018](#); [Wang & Bourouiba 2021](#)). This stems from the expansion of the ligament at the equator. Therefore, the observed breakup mechanisms are quite similar to the findings in the works of [Wang et al. \(2018\)](#) and [Wang & Bourouiba \(2022\)](#). For instance, it is observed that larger values of $1/R$ (thinner lamella thickness, as evidenced in [figure 11](#)) and E_0 (faster expansion speed, as evidenced in §4.3) correspond to finer liquid fingers. Regarding the number of liquid fingers (implies distance between fingers), it is evident that they increase with an increase in E_0 . In contrast, for different $1/R$ cases, the number of liquid fingers remains relatively consistent.

From the quantitative results, it can be observed that, for all cases, the breakup of the liquid fingers follows the instability mechanism known as Stokes flow instability ([Bentley & Leal 1986](#); [Stone 1994](#)). Specifically, it shows short-wave pinching with a wavelength of approximately $\lambda_{fl}/r_{fl} \sim 3.2$, where λ_{fl} and r_{fl} are the wavelength and radius of the liquid fingers ([Shinjo & Umemura 2010](#)). This type of short-wave pinching is a common mechanism for viscous droplets in shear flows ([Wang & Bourouiba 2018](#)). Additionally, it should be noted that, compared with the instability waves on the liquid ring, the spacing between liquid fingers is more uniform, and the sizes between the liquid fingers are also similar. This implies that the satellite droplets produced by fingering breakup have a more uniform size distribution than those generated by liquid ring rupture. It should be noted that the fragmentation of liquid fingers is a highly complex process, especially in terms of its theoretical modelling. [Wang & Bourouiba \(2017, 2018, 2023\)](#) and [Wang et al. \(2018\)](#) provided insightful studies on the fragmentation of liquid fingers generated by droplet impact and derived precise governing equations along with analytical solutions to describe this process. Integrating the observed fingering equatorial streaming with previous instability models ([López-Herrera & Ganan-Calvo 2004](#); [Wang & Bourouiba 2018](#)) to build theoretical equations that can describe the finger's width, breakup length and number would be a fascinating topic for future research. This topic deserves a dedicated paper, which is beyond the present work.

As a summary, all simulation cases are compiled into a phase diagram, as depicted in [figure 20](#). As explained earlier, the occurrence of fingering equatorial streaming can be attributed to two conditions: (i) the larger electric field force, accelerating the expansion of the droplet in the equatorial plane, which is related to $\sim Ca_e$. (ii) The liquid ring detaches rapidly at the equator. Utilizing the dimensionless numbers and power-law relation in §4.3, we have $\sim (Ca_e R/S)^{-0.77}$. Therefore, the functions used to describe the finger-like breakup and ring rupture can be written as

$$32Ca_e + 0.2 \left(\frac{Ca_e R}{S} \right)^{-0.77} = K. \quad (4.6)$$

In this paper, the fitted constant K is set to 160. As evident from the graph, the phase boundary proposed in this study aligns remarkably well with the simulation results and previous experimental findings. The phase diagram obtained can provide guidance for accurately controlling the various breakup mechanisms of droplet equatorial streaming.

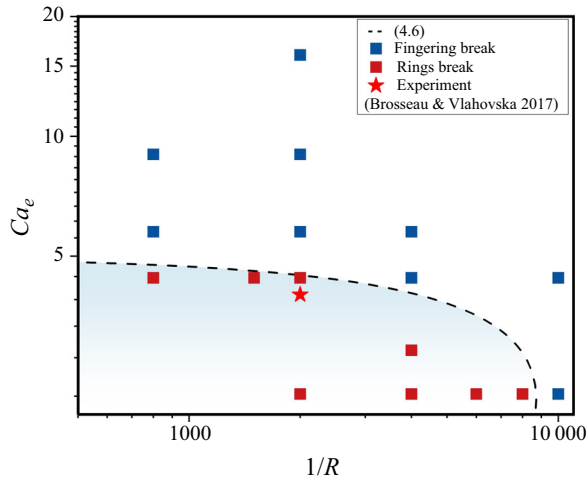


Figure 20. The phase diagram illustrates the results of droplet equatorial streaming, the dashed line represents (4.6).

Additionally, we hope that future experimental research over a larger parameter range will complement our findings about fingering equatorial streaming.

5. Conclusion

Since the discovery of droplet equatorial streaming by Brosseau & Vlahovska (2017), there remain many mysteries behind this phenomenon. The present research has successfully constructed a ULBM multiphase model for EHD to simulate the entire process of droplet equatorial streaming, providing fresh insights. The focus of this paper revolves around three questions: (i) the flow patterns of droplet equatorial streaming in a broader range of parameters than in the experiment, (ii) the dynamic evolution of key parameters during the droplet equatorial streaming and (iii) the underlying mechanisms of fragmentation in the process of droplet equatorial streaming.

Firstly, based on the ULBM framework proposed by Luo *et al.* (2021), we construct a novel multiphase EHD LB model considering charge relaxation and charge convection. For the modelling of multiphase flow, the highly efficient non-orthogonal MRT phase-field LB model recently proposed by Wang *et al.* (2023) is adopted. A ULBM (NMRT) model is developed for charge relaxation and convection. A new source term is introduced to consider the coupling of the charge conservation equation for charge transportation and the Poisson equation for the electric field. Subsequently, the proposed model is comprehensively validated by comparing the simulation results with analytical solutions, previous simulation results and experiments. Notably, the Coulomb fission of droplets in an electric field is successfully reproduced using the LB model, demonstrating excellent agreement with experimental results.

Subsequently, the proposed LB model is applied to simulate the droplet equatorial streaming. Our model has successfully reproduced the entire process observed in experiments, including the continuous ejection of liquid rings at the equator, the fragmentation of the liquid rings and the formation of satellite droplets. Then the physical parameters in our simulations are extended to a broader range than in existing experiments (Brosseau & Vlahovska 2017) and simulations (Wagoner *et al.* 2020, 2021). Under the conditions of high electric field strength and conductivity differences, a novel fingering

equatorial streaming phenomenon is observed. In fingering equatorial streaming, satellite droplets are directly ejected from the liquid fingers at the equator of the mother droplet rather than the breakup of the liquid rings.

The dynamic behaviours of the droplet before the first liquid ring detaches have been investigated. A power-law relationship is first found to exist between the total charge Q_e of the droplet and the evolution time (4.1). Subsequently, a theoretical model (4.4) is developed to describe the time evolution of the droplet radius and height. Our theoretical model shows excellent consistency with the simulation results. Moreover, the critical moments of the first ring detachment are investigated. For all simulated cases, it is found that Q_e at this moment is approximately 2.5 times the Rayleigh limit q_c , with the carried charge of the liquid ring constituting approximately 15%~30% of the total charge. Additionally, for cases with electric field strength $E_0 > E_c$, a power-law decay relationship is observed between the droplet's critical breakup time (4.5). Conversely, for the cases with $E_0 < E_c$, a novel charge accumulation hysteresis phenomenon is discovered.



Finally, we investigate the breakup mechanisms in the droplet equatorial streaming. It is found that the fragmentation of the liquid rings is caused by capillary instability, with the wavelength of unstable waves on the liquid rings and the interval of ring detachment decreasing with the increase in conductivity contrast ($1/R$) and E_0 . The fragmentation of liquid fingers is governed by the end-pinching mechanism. Concerning the size distribution of satellite droplets in the equatorial flow, a reduction in the average radius of satellite droplets with increasing $1/R$ and E_0 is observed, and the size distribution narrowed with increasing $1/R$ but widened with increasing E_0 . This is attributed to the occurrence of fingering equatorial streaming for cases of large E_0 . Based on the mechanism behind the occurrence of fingering equatorial streaming, i.e. (i) high frequency of the liquid ring detachment and (ii) large external electric field forces, we establish a criterion equation (4.6) to distinguish between droplet fingering equatorial streaming and ring equatorial streaming. It is noted that the research on droplet equatorial flow is still in its early stages, and its comprehensive understanding requires extensive experimental and simulation studies (Vlahovska 2019; Wagoner *et al.* 2021). While qualitative analysis for liquid rings and liquid fingers under different E_0 and $1/R$ are provided in § 4.4, further theoretical modelling is necessary. Constructing a theoretical model that accurately describes the instabilities in equatorial streaming including the fingering instability merits further exploration.

Supplemental material and movies. Supplementary material and movies are available at <https://doi.org/10.1017/jfm.2024.441>.

Funding. Support from the UK Engineering and Physical Sciences Research Council under the project 'UK Consortium on Mesoscale Engineering Sciences (UKCOMES)' (grant no. EP/X035875/1) is gratefully acknowledged. This work made use of computational support by CoSeC, the Computational Science Centre for Research Communities, through UKCOMES.

Declaration of interests. The authors report no conflict of interest.

Author ORCIDs.

-  Timan Lei <https://orcid.org/0000-0002-8031-6632>;
-  Junyu Yang <https://orcid.org/0000-0002-7771-1308>;
-  Linlin Fei <https://orcid.org/0000-0002-4722-5093>;
-  Jin Chen <https://orcid.org/0009-0005-5844-635X>;
-  Kai H. Luo <https://orcid.org/0000-0003-4023-7259>.

REFERENCES

- ABBASI, M.S., SONG, R., KIM, S.M., KIM, H. & LEE, J. 2019 Mono-emulsion droplet stretching under direct current electric field. *Soft Matt.* **15** (11), 2328–2335.
- ACHTZEHN, T., MÜLLER, R., DUFT, D. & LEISNER, T. 2005 The Coulomb instability of charged microdroplets: dynamics and scaling. *Eur. Phys. J. D* **34** (1–3), 311–313.
- ALLAN, R.S., MASON, S.G. & MARION, L.E. 1962 Particle behaviour in shear and electric fields I. Deformation and burst of fluid drops. *Proc. R. Soc. London. Ser. A. Math. Phys. Sci.* **267** (1328), 45–61.
- ALLEN, S.M. & CAHN, J.W. 1979 A microscopic theory for antiphase boundary motion and its application to antiphase domain coarsening. *Acta Metall.* **27** (6), 1085–1095.
- BENTLEY, B.J. & LEAL, L.G. 1986 An experimental study of transient effects in the breakup of viscous drops. *J. Fluid Mech.* **173**, 131–158.
- BETELÚ, S.I., FONTELOS, M.A., KINDELÁN, U. & VANTZOS, O. 2006 Singularities on charged viscous droplets. *Phys. Fluids* **18** (5), 1–5.
- BÖSCH, F., CHIKATAMARLA, S.S. & KARLIN, I.V. 2015 Entropic multirelaxation lattice Boltzmann models for turbulent flows. *Phys. Rev. E* **92**, 043309.
- BROSSEAU, Q. & VLAHOVSKA, P.M. 2017 Streaming from the equator of a drop in an external electric field. *Phys. Rev. Lett.* **119** (3), 034501.
- BURTON, J.C. & TABOREK, P. 2011 Simulations of coulombic fission of charged inviscid drops. *Phys. Rev. Lett.* **106** (14), 1–4.
- CAI, S., SUN, Y., WANG, Z., YANG, W., LI, X. & YU, H. 2021 Mechanisms, influencing factors, and applications of electrohydrodynamic jet printing. *Nanotechnol. Rev.* **10** (1), 1046–1078.
- CHAI, Z. & SHI, B. 2008 A novel lattice Boltzmann model for the Poisson equation. *Appl. Math. Model.* **32** (10), 2050–2058.
- COLLINS, R.T., JONES, J.J., HARRIS, M.T. & BASARAN, O.A. 2008 Electrohydrodynamic tip streaming and emission of charged drops from liquid cones. *Nat. Phys.* **4** (2), 149–154.
- COLLINS, R.T., SAMBATH, K., HARRIS, M.T. & BASARAN, O.A. 2013 Universal scaling laws for the disintegration of electrified drops. *Proc. Natl Acad. Sci. USA* **110** (13), 4905–4910.
- CUI, Y., WANG, N. & LIU, H. 2019 Numerical study of droplet dynamics in a steady electric field using a hybrid lattice Boltzmann and finite volume method. *Phys. Fluids* **31** (2), 022105.
- DUFT, D., ACHTZEHN, T., MÜLLER, R., HUBER, B.A. & LEISNER, T. 2003 Rayleigh jets from levitated microdroplets. *Nature* **421** (6919), 128–128.
- EGGLETON, C.D., TSAI, T.M. & STEBE, K.J. 2001 Tip streaming from a drop in the presence of surfactants. *Phys. Rev. Lett.* **87** (4), 48302-1–48302-4.
- ESMAEELI, A. & SHARIFI, P. 2011 Transient electrohydrodynamics of a liquid drop. *Phys. Rev. E - Stat. Nonlinear Soft Matt. Phys.* **84** (3), 1–11.
- FEI, L., DU, J., LUO, K.H., SUCCI, S., LAURICELLA, M., MONTESSORI, A. & WANG, Q. 2019 Modeling realistic multiphase flows using a non-orthogonal multiple-relaxation-time lattice Boltzmann method. *Phys. Fluids* **31** (4), 042105.
- FEI, L. & LUO, K.H. 2017 Consistent forcing scheme in the cascaded lattice Boltzmann method. *Phys. Rev. E* **96** (5), 053307.
- FEI, L., LUO, K.H. & LI, Q. 2018 Three-dimensional cascaded lattice Boltzmann method: improved implementation and consistent forcing scheme. *Phys. Rev. E* **97** (5), 053309.
- FEI, L., QIN, F., ZHAO, J., DEROME, D. & CARMELIET, J. 2023 Lattice Boltzmann modelling of isothermal two-component evaporation in porous media. *J. Fluid Mech.* **955**, A18.
- FENG, J.Q. 2002 A 2D electrohydrodynamic model for electrorotation of fluid drops. *J. Colloid Interface Sci.* **246** (1), 112–121.
- FENN, J.B., MANN, M., MENG, C.K., WONG, S.F. & WHITEHOUSE, C.M. 1989 Electrospray ionization for mass spectrometry of large biomolecules. *Science*. **246** (4926), 64–71.
- FENN, J.B., MANN, M., MENG, C.K., WONG, S.F. & WHITEHOUSE, C.M. 1990 Electrospray ionization—principles and practice. *Mass Spectrom. Rev.* **9** (1), 37–70.
- FERNÁNDEZ DE LA MORA, J. 2007 The fluid dynamics of Taylor cones. *Annu. Rev. Fluid Mech.* **39** (1), 217–243.
- FIROUZIAN, M., MIKSI, M.J., VLAHOVSKA, P.M. & SAINTILLAN, D. 2022 Instability of a planar fluid interface under a tangential electric field in a stagnation point flow. *J. Fluid Mech.* **931**, 1–23.
- GAÑÁN-CALVO, A.M. 1999 The surface charge in electrospaying: its nature and its universal scaling laws. *J. Aerosol Sci.* **30** (7), 863–872.
- GAÑÁN-CALVO, A.M., LÓPEZ-HERRERA, J.M., HERRADA, M.A., RAMOS, A. & MONTANERO, J.M. 2018 Review on the physics of electrospray: from electrokinetics to the operating conditions of single and coaxial Taylor cone-jets, and AC electrospray. *J. Aerosol Sci.* **125**, 32–56.

- GAÑÁN-CALVO, A.M., LÓPEZ-HERRERA, J.M., REBOLLO-MUÑOZ, N. & MONTANERO, J.M. 2016 The onset of electrospray: the universal scaling laws of the first ejection. *Sci. Rep.* **6**, 1–9.
- GARZON, M., GRAY, L.J. & SETHIAN, J.A. 2014 Numerical simulations of electrostatically driven jets from nonviscous droplets. *Phys. Rev. E - Stat. Nonlinear Soft Matt. Phys.* **89** (3), 1–16.
- GAWANDE, N., MAYYA, Y.S. & THAOKAR, R. 2017 Numerical study of Rayleigh fission of a charged viscous liquid drop. *Phys. Rev. Fluids* **2** (11), 113603.
- GAWANDE, N., MAYYA, Y.S. & THAOKAR, R. 2019 Jet and progeny formation in the Rayleigh breakup of a charged viscous drop. *J. Fluid Mech.* **884**, A31.
- GAWANDE, N., MAYYA, Y.S. & THAOKAR, R. 2022 Effect of conductivity on the mechanism of charge ejection in Rayleigh breakup of a charged drop. *J. Electrostat.* **117**, 103720.
- GIGLIO, E., GERVAIS, B., RANGAMA, J., MANIL, B., HUBER, B.A., DUFT, D., MÜLLER, R., LEISNER, T. & GUET, C. 2008 Shape deformations of surface-charged microdroplets. *Phys. Rev. E - Stat. Nonlinear Soft Matt. Phys.* **77** (3), 1–7.
- GONG, S., CHENG, P. & QUAN, X. 2010 Lattice Boltzmann simulation of droplet formation in microchannels under an electric field. *Intl J. Heat Mass Transfer* **53** (25), 5863–5870.
- GRIMM, R.L. & BEAUCHAMP, J.L. 2005 Dynamics of field-induced droplet ionization: time-resolved studies of distortion, jetting, and progeny formation from charged and neutral methanol droplets exposed to strong electric fields. *J. Phys. Chem. B* **109** (16), 8244–8250.
- HA, J.W. & YANG, S.M. 2000 Deformation and breakup of Newtonian and non-Newtonian conducting drops in an electric field. *J. Fluid Mech.* **405**, 131–156.
- HARRIS, M.T., SCOTT, T.C. & BYERS, C.H. 1993 The synthesis of metal hydrous oxide particles by multiphase electrodispersion. *Mater. Sci. Engng A* **168** (2), 125–129.
- HERRADA, M.A., LÓPEZ-HERRERA, J.M., GAÑÁN-CALVO, A.M., VEGA, E.J., MONTANERO, J.M. & POPINET, S. 2012 Numerical simulation of electrospray in the cone-jet mode. *Phys. Rev. E - Stat. Nonlinear Soft Matt. Phys.* **86** (2), 1–8.
- JAIN, S.S. 2022 Accurate conservative phase-field method for simulation of two-phase flows. *J. Comput. Phys.* **469**, 111529.
- KARLIN, I.V., BÖSCH, F. & CHIKATAMARLA, S.S. 2014 Gibbs' principle for the lattice-kinetic theory of fluid dynamics. *Phys. Rev. E* **90** (3), 031302.
- KARYAPPA, R.B., DESHMUKH, S.D. & THAOKAR, R.M. 2014 Breakup of a conducting drop in a uniform electric field. *J. Fluid Mech.* **754** (3), 550–589.
- KOOIJ, S.A., MOQADDAM, A.M., DE GOEDE, T.C., DEROME, D., CARMELIET, J., SHAHIDZADEH, N. & BONN, D. 2019 Sprays from droplets impacting a mesh. *J. Fluid Mech.* **871**, 489–509.
- LEI, T., WANG, Z. & LUO, K.H. 2021 Study of pore-scale coke combustion in porous media using lattice Boltzmann method. *Combust. Flame* **225**, 104–119.
- LI, N., PANG, Y., SUN, Z., SUN, Y., QI, Z., LI, W., LIU, Y., LI, B., WANG, Z. & ZENG, H.B. 2023 Electric field-induced deformation and breakup of water droplets in polymer-flooding W/O emulsions: a simulation study. *Sep. Purif. Technol.* **320**, 124237.
- LI, Q., LUO, K.H., KANG, Q.J., HE, Y.L., CHEN, Q. & LIU, Q. 2016 Lattice Boltzmann methods for multiphase flow and phase-change heat transfer. *Prog. Energy Combust. Sci.* **52**, 62–105.
- LIANG, H., WANG, R., WEI, Y. & XU, J. 2023 Lattice Boltzmann method for interface capturing. *Phys. Rev. E* **107** (2), 025302.
- LIU, X., CHAI, Z. & SHI, B. 2019 A phase-field-based lattice Boltzmann modeling of two-phase electro-hydrodynamic flows. *Phys. Fluids* **31** (9), 092103.
- LÓPEZ-HERRERA, J.M. & GANAN-CALVO, A.M. 2004 A note on charged capillary jet breakup of conducting liquids: experimental validation of a viscous one-dimensional model. *J. Fluid Mech.* **501**, 303–326.
- LÓPEZ-HERRERA, J.M., GAÑÁN-CALVO, A.M., POPINET, S. & HERRADA, M.A. 2015 Electrokinetic effects in the breakup of electrified jets: a volume-of-fluid numerical study. *Intl J. Multiphase Flow* **71**, 14–22.
- LÓPEZ-HERRERA, J.M., HERRADA, M.A. & GAÑÁN-CALVO, A.M. 2023 Electrokinetic modelling of cone-jet electrosprays. *J. Fluid Mech.* **964**, 1–24.
- LÓPEZ-HERRERA, J.M., POPINET, S. & HERRADA, M.A. 2011 A charge-conservative approach for simulating electrohydrodynamic two-phase flows using volume-of-fluid. *J. Comput. Phys.* **230** (5), 1939–1955.
- LUO, K., WU, J., YI, H.L. & TAN, H.P. 2016 Lattice Boltzmann model for Coulomb-driven flows in dielectric liquids. *Phys. Rev. E* **93** (2), 1–11.
- LUO, K., WU, J., YI, H.L. & TAN, H.P. 2020 Numerical analysis of two-phase electrohydrodynamic flows in the presence of surface charge convection. *Phys. Fluids* **32**, 12.

- LUO, K.H., FEI, L. & WANG, G. 2021 A unified lattice Boltzmann model and application to multiphase flows. *Phil. Trans. R. Soc. A Math. Phys. Engng Sci.* **379** (2208), 20200397.
- LUO, X., YAN, H., HUANG, X., YANG, D., WANG, J. & HE, L. 2017 Breakup characteristics of aqueous droplet with surfactant in oil under direct current electric field. *J. Colloid Interface Sci.* **505**, 460–466.
- MANDAL, S. & CHAKRABORTY, S. 2017 Uniform electric-field-induced non-Newtonian rheology of a dilute suspension of deformable Newtonian drops. *Phys. Rev. Fluids* **2** (9), 1–30.
- MANDAL, S., CHAUDHURY, K. & CHAKRABORTY, S. 2014 Transient dynamics of confined liquid drops in a uniform electric field. *Phys. Rev. E - Stat. Nonlinear Soft Matt. Phys.* **89** (5), 1–17.
- MARIN, A. 2020 The Saturnian droplet. *J. Fluid Mech.* **908**, 1–4.
- MELCHER, J.R. & TAYLOR, G.I. 1969 Electrohydrodynamics: a review of the role of interfacial shear stresses. *Annu. Rev. Fluid Mech.* **1** (1), 111–146.
- MISRA, K. & GAMERO-CASTAÑO, M. 2023 Ion emission from nanodroplets undergoing Coulomb explosions: a continuum numerical study. *J. Fluid Mech.* **958**, A32.
- MOHAMED, A.S., LOPEZ-HERRERA, J.M., HERRADA, M.A., MODESTO-LOPEZ, L.B. & GAÑÁN-CALVO, A.M. 2016 Effect of a surrounding liquid environment on the electrical disruption of pendant droplets. *Langmuir* **32** (27), 6815–6824.
- PTASINSKI, K.J. & KERKHOFF, P.J.A.M. 1992 Electric field driven separations: phenomena and applications. *Sep. Sci. Technol.* **27** (8–9), 995–1021.
- RAYLEIGH, LORD 1878 On the instability of jets. *Proc. Lond. Math. Soc.* **s1-10** (1), 4–13.
- RAYLEIGH, LORD 1882 XX. On the equilibrium of liquid conducting masses charged with electricity. *London Edinburgh Dublin Phil. Mag. J. Sci.* **14** (87), 184–186.
- REZNIK, S.N., YARIN, A.L., THERON, A. & ZUSSMAN, E. 2004 Transient and steady shapes of droplets attached to a surface in a strong electric field. *J. Fluid Mech.* **516**, 349–377.
- SENGUPTA, R., WALKER, L.M. & KHAIR, A.S. 2017 The role of surface charge convection in the electrohydrodynamics and breakup of prolate drops. *J. Fluid Mech.* **833**, 29–53.
- SHINJO, J. & UMEMURA, A. 2010 Simulation of liquid jet primary breakup: dynamics of ligament and droplet formation. *Intl J. Multiphase Flow* **36** (7), 513–532.
- STONE, H.A. 1994 Dynamics of drop deformation and breakup in viscous fluids. *Annu. Rev. Fluid Mech.* **26** (1), 65–102.
- STUART, J.T. 1985 Dynamics of charged drop break-up. *Proc. R. Soc. Lond. A Math. Phys. Sci.* **401** (1820), 67–88.
- TAYLOR, G.I. 1964 Disintegration of water drops in an electric field. *Proc. R. Soc. Lond. Ser. A. Math. Phys. Sci.* **280** (1382), 383–397.
- TAYLOR, G.I., MCEWAN, A.D. & DE JONG, L.N.J. 1966 Studies in electrohydrodynamics. I. The circulation produced in a drop by an electric field. *Proc. R. Soc. Lond. A Math. Phys. Sci.* **291** (1425), 159–166.
- TIAN, Y., WANG, H., ZHOU, X., XIE, Z., ZHU, X., XIE, Z., ZHU, X., CHEN, R., DING, Y. & LIAO, Q. 2022 How does the electric field make a droplet exhibit the ejection and rebound behaviour on a superhydrophobic surface? *J. Fluid Mech.* **941**, 1–29.
- TOMAR, G., GERLACH, D., BISWAS, G., ALLEBORN, N., SHARMA, A., DURST, F., WELCH, S.W. & DELGADO, A. 2007 Two-phase electrohydrodynamic simulations using a volume-of-fluid approach. *J. Comput. Phys.* **227** (2), 1267–1285.
- TOMOTIKA, S. 1935 On the instability of a cylindrical thread of a viscous liquid surrounded by another viscous fluid. *Proc. R. Soc. Lond. A Math. Phys. Sci.* **150** (870), 322–337.
- UNVERDI, S.O. & TRYGGVASON, G. 1992 A front-tracking method for viscous, incompressible, multi-fluid flows. *J. Comput. Phys.* **100** (1), 25–37.
- VILLERMAUX, E., MARMOTTANT, P. & DUPLAT, J. 2004 Ligament-mediated spray formation. *Phys. Rev. Lett.* **92** (7), 1–4.
- VLAHOVSKA, P.M. 2019 Electrohydrodynamics of drops and vesicles. *Annu. Rev. Fluid Mech.* **51**, 305–330.
- WAGONER, B.W., VLAHOVSKA, P.M., HARRIS, M.T. & BASARAN, O.A. 2020 Electric-field-induced transitions from spherical to discocyte and lens-shaped drops. *J. Fluid Mech.* **904**, 1–15.
- WAGONER, B.W., VLAHOVSKA, P.M., HARRIS, M.T. & BASARAN, O.A. 2021 Electrohydrodynamics of lenticular drops and equatorial streaming. *J. Fluid Mech.* **925**, 1–23.
- WANG, G., FEI, L., LEI, T., WANG, Q. & LUO, K.H. 2022a Droplet impact on a heated porous plate above the Leidenfrost temperature: a lattice Boltzmann study. *Phys. Fluids* **34** (9), 93319.
- WANG, G., FEI, L. & LUO, K.H. 2022b Unified lattice Boltzmann method with improved schemes for multiphase flow simulation: application to droplet dynamics under realistic conditions. *Phys. Rev. E* **105** (4), 045314.

Lattice Boltzmann modelling

- WANG, G., YANG, J., LEI, T., CHEN, J., WANG, Q. & LUO, K.H. 2023 A three-dimensional non-orthogonal multiple-relaxation-time phase-field lattice Boltzmann model for multiphase flows at large density ratios and high Reynolds numbers. *Intl J. Multiphase Flow* **168**, 104582.
- WANG, Y. & BOUROUIBA, L. 2017 Drop impact on small surfaces: thickness and velocity profiles of the expanding sheet in the air. *J. Fluid Mech.* **814**, 510–534.
- WANG, Y. & BOUROUIBA, L. 2018 Unsteady sheet fragmentation: droplet sizes and speeds. *J. Fluid Mech.* **848**, 946–967.
- WANG, Y. & BOUROUIBA, L. 2021 Growth and breakup of ligaments in unsteady fragmentation. *J. Fluid Mech.* **910**, A39.
- WANG, Y. & BOUROUIBA, L. 2022 Mass, momentum and energy partitioning in unsteady fragmentation. *J. Fluid Mech.* **935**, A29.
- WANG, Y. & BOUROUIBA, L. 2023 Non-Galilean Taylor–Culick law governs sheet dynamics in unsteady fragmentation. *J. Fluid Mech.* **969**, A19.
- WANG, Y., DANDEKAR, R., BUSTOS, N., POULAIN, S. & BOUROUIBA, L. 2018 Universal rim thickness in unsteady sheet fragmentation. *Phys. Rev. Lett.* **120** (20), 204503.
- YANG, J., FEI, L., ZHANG, X., MA, X., LUO, K.H. & SHUAI, S. 2021 Dynamic behavior of droplet transport on realistic gas diffusion layer with inertial effect via a unified lattice Boltzmann method. *Intl J. Hydrogen Energy* **46** (66), 33260–33271.
- ZHANG, J. & KWOK, D.Y. 2005 A 2D lattice Boltzmann study on electrohydrodynamic drop deformation with the leaky dielectric theory. *J. Comput. Phys.* **206** (1), 150–161.
- ZHANG, W., WANG, J., WANG, Z., LI, B., YU, K., ZHAN, S., HUO, Y., WANG, H. & XU, H. 2023 Review of bubble dynamics on charged liquid-gas flow. *Phys. Fluids* **35** (2), 021302.
- ZHAO, S. & TAO, J. 2016 Weakly nonlinear instabilities of a liquid ring. *Phys. Fluids* **28** (11), 114104.